2008

Magneto-optical study of the intermediate state in type-I superconductors: effects of sample shape and applied current

Jacob Ray Hoberg
Iowa State University

Magneto-optical study of the intermediate state in type-I superconductors: effects of sample shape and applied current

by

Jacob Ray Hoberg

A thesis submitted to the graduate faculty

in partial fulfillment of the requirements for the degree of

MASTER OF SCIENCE

Major: Condensed Matter Physics

Program of Study Committee:
Ruslan Prozorov, Major Professor
Paul C. Canfield
Scott Chumbley
Edward Yu
Charles R. Kerton

Iowa State University

Ames, Iowa

2008

TABLE OF CONTENTS

LIST OF FIGURES

ABSTRACT

The magnetic flux structures in the intermediate state of bulk, pinning-free Type-I superconductors are studied using a high resolution magneto-optical imaging technique. Unlike most previous studies, this work focuses on the pattern formation of the coexisting normal and superconducting phases in the intermediate state. The influence of various parameters such as sample shape, structure defects (pinning) and applied current are discussed in relation to two distinct topologies: flux tubes (closed topology) and laminar (open topology). Imaging and magnetization measurements performed on samples of different shapes (cones, hemispheres and slabs), show that contrary to previous beliefs, the tubular structure is the equilibrium topology, but it is unstable toward defects and flux motion. Moreover, the application of current into a sample with the geometric barrier can replace an established laminar structure with flux tubes. At very high currents, however, there exists a laminar "stripe pattern." Quantitative analysis of the mean tube diameter is shown to be in good agreement with the prediction proposed by Goren and Tinkham. This is the first time that this model has been confirmed experimentally. Further research into the flux tube phase shows a direct correlation with the current loop model proposed in the 1990's by Goldstein, Jackson and Dorsey. There also appears a range of flux tube density that results in a suprafroth structure, a well-formed polygonal mesh, which behaves according to the physics of foams, following standard statistical laws such as von Neumann and Lewis. The reaction of flux structures to a fast-ramped magnetic field was also studied. This provided an alignment of the structure not normally observed at slow ramp rates.

CHAPTER I. INTRODUCTION

Since Landau first described the intermediate state in Type-I superconductors in 1937[1], the magnetic structures of this state have been of ceaseless interest. Due to the complex competition in energy terms in this system, there is an incomplete understanding of these structures. Similar pattern formations have been found in a multitude of systems ranging from neutron stars[2,3] to dipolar fluids[4] to vegetation patterns[5], along with many others[6-12]. All of these different research areas exhibit similarities in patterns. Because of these similarities, our studies of the intermediate state of Type-I superconductors are vital in the overall understanding of these pattern formations. This research has been performed to further understand the magnetic structures in the intermediate state along with the energy contributions that define them.

1. Type-I vs. Type-II Superconductors

Superconductivity was first discovered in 1911[13] when the resistivity of mercury (Hg) dropped to zero at temperatures below 4.15 K. Since then, superconductors have been found to have two fundamental properties: perfect diamagnetism and perfect conductivity. Many theories were proposed to explain this phenomenon, notably the Ginzburg-Landau theory[14] in 1950 and shortly afterwards, the BCS theory[14] was put forth by Bardeen, Cooper and Schrieffer in 1957. BCS theory is the generally accepted explanation of superconductivity.

There are two fundamentally different superconductor groups labeled Type-I and Type-II. These groups can be classified in many ways, but for the purpose of this thesis I'll consider their respective responses to an applied magnetic field. In both superconductor types there is perfect diamagnetism. An applied field is perfectly screened beyond a London

penetration depth[13]. For an ideal Type-I superconductor, this remains so until the applied field reaches a critical field, H_c, when it becomes energetically favorable for the material to become normal and allow a full penetration of the applied field. In a Type-II superconductor[15], there is a similar applied field, H_{c2}, which drives the system completely normal. However, for Type-II superconductors, there exists an intermediate field, H_{c1}, at which the system enters the "mixed state."

The mixed state appears in Type-II superconductors because it is energetically favorable. In zero field, the energy gained[13] by a superconducting transition from the normal state is $f_n(T) - f_s(T) = H_c^2(T)/8\pi$, where $f_n(T)$ and $f_s(T)$ are the free energy densities of the normal and superconducting states, respectively. Beyond an applied field of H_{c1}, however, we must consider the superconducting-normal state (S-N) domain wall energy for penetration of the magnetic field in the mixed state (the intermediate state will be discussed shortly). The superconducting electrons do not break their Cooper pairs abruptly at the S-N interface. Instead, this breaking occurs over a distance known as the coherence length, ξ. This distance results in a positive contribution to the wall energy, $(H_c^2/8\pi)\xi$. Also, the magnetic field

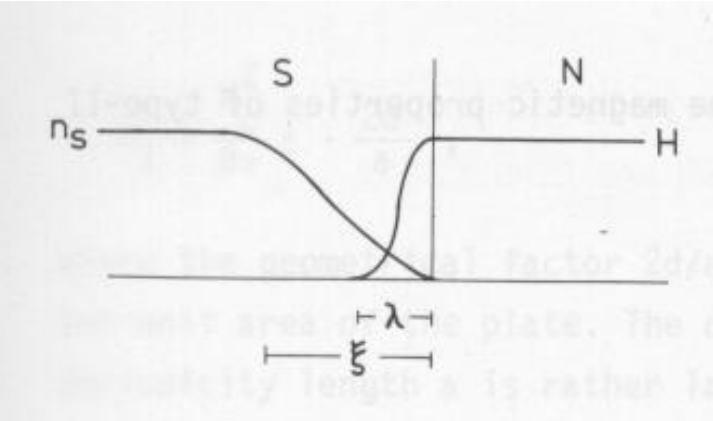

Figure 1. Domain Wall Energy. The image shows a typical Type-I superconducting wall energy. *H* is the applied field, *N* is the normal state, S is the superconducting state, and n_s is the density of superconducting electrons.

from the normal side of the interface penetrates a depth λ (thusly named the "penetration depth") into the superconducting region. This magnetic field penetration provides a decrease in the wall energy of $(H_c^2/8\pi)\lambda$. The overall wall energy[13] is therefore described as $\alpha = (H_c^2/8\pi)(\xi - \lambda)$. Figure 1 depicts this competition of energies. The penetration depth λ is smaller than the coherence length ξ inside a Type-I superconductor. This occurrence results in a superconducting-normal state domain wall with positive energy. For a Type-II superconductor with negative wall energy, it is energetically favorable to create these domain walls. The result is the mixed state, a combination of both the Meissner state and normal state tubes containing single flux quanta called Abrikosov vortices[14]. Because each barrier between the superconducting and normal states lowers the total energy, the system prefers these tubes of single flux quanta.

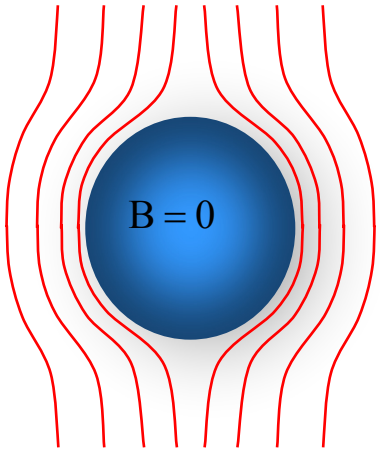

Figure 2. Perfect Diamagnetism.

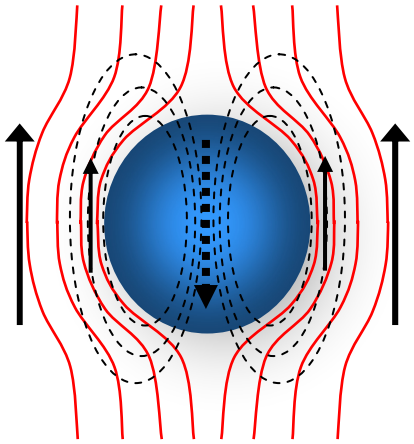

Figure 3. Increased H_c. The solid lines represent the applied field. The dashed lines represent the magnetization from the supercurrents.

The mixed state at applied fields (H_a) where $H_{c1} < H_a < H_{c2}$ is what distinguishes Type-II from Type-I in general. However, Type-I superconductors also have an interesting feature at intermediate fields. While it's true that superconductors have perfect diamagnetism, only ideal systems (i.e. long, straight wires with the field applied along the axis) have an immediate transition into the normal state. The expulsion of flux (Figure 2)

inside a superconductor arises from the diamagnetic effect in combination with the perfect conductivity. The diamagnetic effect creates supercurrents[14] that create an internal magnetization that opposes the applied field completely. And because there is no resistance, the supercurrents require very little energy. However, the magnetization created to oppose an overall field inside the sample must close on itself, and does so by circling outside of the sample (Figure 3). This added field creates an edge field[13], $H_e = H_a + H_M = H_a/(1-N)$, where H_M is the external field resulting from the internal magnetization and N is the demagnetization coefficient. This higher edge field becomes a concern as the H_e approaches H_c for a Type-I superconductor. When $H_e = H_c$, the sample should go normal, but if the sample becomes normal then the supercurrents disappear along with their contribution to the edge field. At that point the edge field is only equal to the applied field and the sample is back in the superconducting state. Rather than cycle between normal and superconducting states, the superconductor allows some of the applied field to penetrate. This introduces the intermediate state in Type-I superconductors.

2. The Intermediate State

The intermediate state is not the same as the mixed state — the former being applied to Type-I superconductors, the latter applied to Type-II superconductors. The intermediate state is not intrinsic in the properties of the superconducting state; it arises purely from the diamagnetic effect of a sample. The true difference between the intermediate state and the mixed state, however, is the S-N domain wall energy, α. For a Type-I superconductor it is

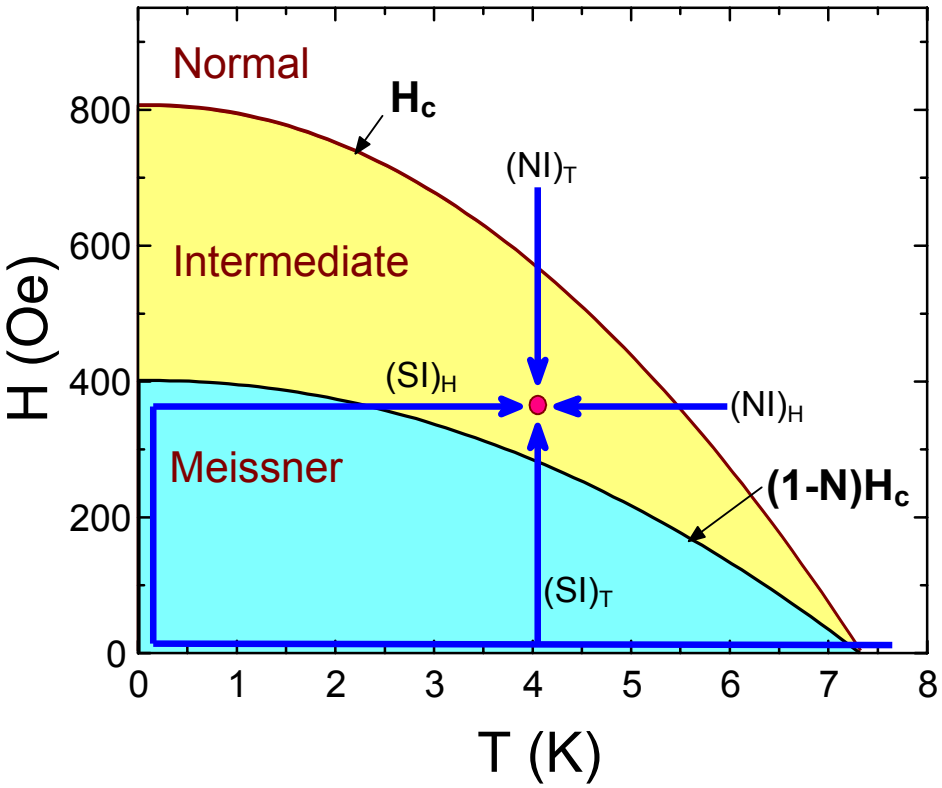

Figure 4. H-T Phase Diagram of a Type-I Superconductor. Each arrow depicts a thermodynamically independent path to approach the same point in the intermediate state.

positive, $\xi > \lambda$. It's this positive addition in the energy that has led to the extensive studies in the pattern formation of the magnetic field in the intermediate state.

Before discussing the details of the intermediate state, let us discuss how to reach this state. To reach the intermediate state, there are four fundamental paths involving a combination of either field cooling (FC) or zero field cooling (ZFC) the sample and either changing the applied field or applied temperature. Each path in Figure 4 depicts one of these methods. Two paths are FC and result from either approaching the intermediate state from an intermediate field and decreasing temperature or approaching from a high field at superconducting temperatures and lowering the field. These two paths have been labeled as NI because they cross from the normal state to the intermediate state. The remaining two

paths are ZFC and are labeled SI as they cross from the superconducting state into the intermediate state. The sample can be cooled to superconducting temperatures in zero field and the field is then increased into the intermediate state. The last path involves cooling the superconductor even further and applying an intermediate field while remaining in the Meissner state, then increasing the temperature again. For these studies, all temperatures will be quoted in Kelvin (K) and all fields in Oersted (Oe). It should also be noted that even though the intermediate state can be produced purely by application of strong currents[16,17], I will not address this method. I will, however, discuss the effects that an applied current has on the flux structure created by an applied field.

Figure 5 shows the measured magnetization loop at 4.5 K for a small Pb sphere. As can be seen, the magnetization of the sphere peaks at $H_c(1-N)$, where $N = 1/3$. Beyond that, the increasing applied field brings about the intermediate state and a decrease in the

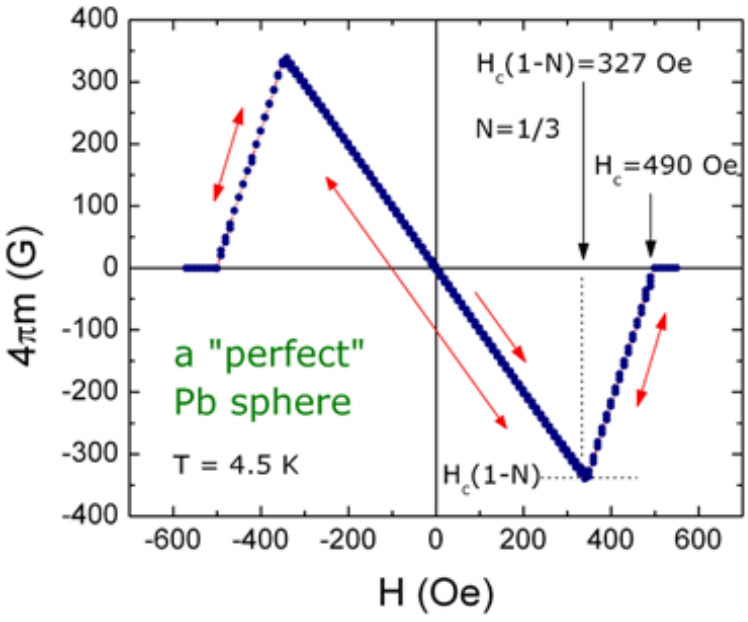

Figure 5. Pb Sphere Magnetization Loop. The Pb sphere measured was ~3 mm in diameter. This loop shows no magnetic hysteresis.

magnitude of the magnetization. The magnetization becomes zero when H_c is reached and the sphere enters the normal state. Also, after a full loop in the magnetization there is no apparent hysteresis is this sample. As this sample shows, the demagnetization factor resulting from the sample shape plays a role in the creation and formation of the intermediate state. The question to be posed is, "how?"

3. Previous Works Performed on Magneto-Optics Imaging of the Intermediate State

Since the 1940's, many groups have performed experiments and imaging on the intermediate state of Type-I superconductors. A bulk of the work has been performed on thin films. For example, Huebener reviews some noteworthy work performed on Lead, Tin and Mercury thin films in his book on magnetic flux structures[13]. Tube nucleation, flux branching and the growth of superconducting domains in laminar structure are all discussed for these experiments. Flux tubes were first discovered in a split Tin sphere by Meshkovsky and Shalnikov[45] in 1947 using bismuth probes. In 1971, an extensive look at the Landau laminar structure was performed by Fortini and Paumier[36]. Fortini and Paumier also studied the effect of sample shape on the field penetration in 1976[46] in an attempt to prove the existence of a "magnetic energy barrier… strictly dependent on the shape of the specimen." This would later be referred to as the geometric barrier, which has been studied at length[30,31,44,47-49]. In 1970, the critical current of the intermediate state was described by Leupold *et al.*[50] while the current-induced flow of magnetic domains was discussed by Solomon and Harris[33]. Shortly following, in 1971, the current-induced intermediate state was examined by Baird and Mukherjee[16].

Recently, in 1996, the current loop model[32] was put forth. This model was then explored extensively by Dorsey and Goldstein in 1998[43] and a comparison between this model and Landau's was made by Reisin and Lipson in 1999[42]. Also in the past few years, Jeudy *et al.* studied magnetic structures containing both tubular and laminar structures[24] and the nucleation of superconducting lines just below H_c[26]. Cebers *et al.* recently (2005) published an extension to the current loop model called the constrained current loop model[25]. Menghini *et al.* have performed some very interesting studies lately. In 2005, they looked at the Type-II regime of Pb[51] and its dendritic formation. Also, they observed the effects of a rotating angled applied field[52] (2005) and the application of an AC field[53] (2007) on the intermediate state structures. In both cases, they found a breaking of the laminar state, specifically a breaking into the tubular structure through application of the AC field. Also in 2005, Hernandez and Dominguez presented simulations of the intermediate state and found both tubular and laminar structures[53].

4. Magneto-Optical Method

Imaging of magnetic structures at the surface of a given sample can be achieved multiple ways. The two most common extrinsic methods have been the Bitter decoration method and the Magneto-Optical (MO) method. The Bitter method utilizes the decorating of ferromagnetic particles on the surface of the sample. These particles are attracted by the largest values of the gradient of the local magnetic field thus making the magnetic structure visible. The Bitter method resolution is dependent on the particle grain size and the sharpness of the field variation.

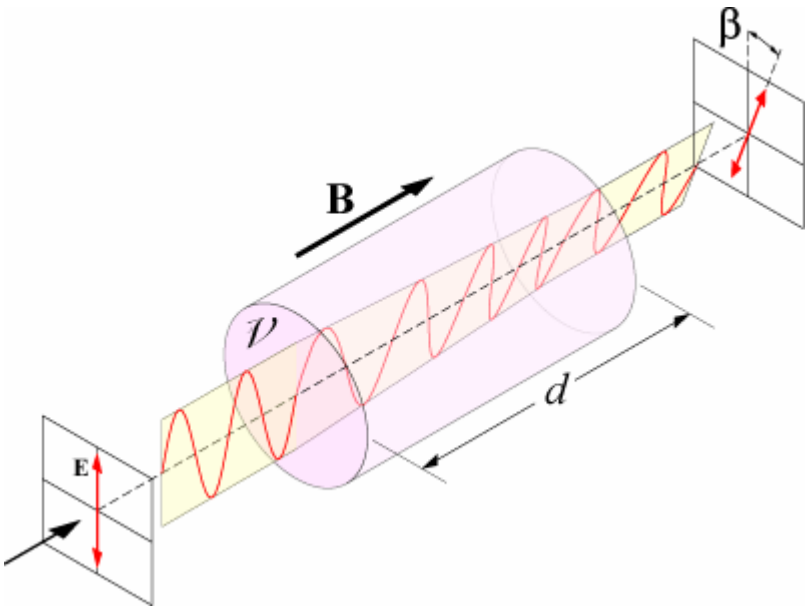

Figure 6. Faraday Rotation. The image shows the effect of a magnetic field on the rotation of polarized light. *B* is the magnetic field, *V* is the Verdet constant, *d* is the length of propogation, and *β* is the angle of rotation.

The MO method utilizes Faraday rotation[19] to image magnetic domains. This method relies on a magneto-optical layer (MOL) rather than magnetic particles and is therefore easier to employ. The MOL can either be placed on top of a sample or directly evaporated onto the sample surface. MO measurements also allow a continuous observation of dynamic phenomena.

Faraday rotation refers to the rotation of polarized light when such light passes through a parallel magnetic field (Figure 6). The rotation angle, *β(H)*, can be described by $\beta = V(\omega) \cdot d \cdot H_z$, where H_z is the magnitude of the applied field along the propagation direction, d is the length of propagation, and *V(ω)* is the Verdet constant[18]. A few commonly used MOL's exist. Jooss[18] describes the use of both paramagnetic EuSe and ferrimagnet bismuth-doped iron garnet films with in-plane magnetization. Huebener[13], however, has an extensive discussion on the uses of EuS, EuSe, and EuO. Cebers *et al.*[25] recently published

work stating the use of indicators made of EuS and CdMnTe, while Castro *et al.*[31] employed EuSe indicators and Menghini and Wijngaarden[52] used yttrium-iron garnet indicators. The research presented in this thesis implemented use of bismuth-doped iron garnet indicators. These indicators have a low spatial resolution, 5 μm, but are usable up to 600 K. Their use will be discussed further in the Experimental Setup chapter.

5. Motivation and Goals

While imaging of the intermediate state of Type-I superconductors has been performed for over 40 years, because of the complex competition in energy terms, the understanding of the structures of the magnetic field in this state is still incomplete. Until recently[20,21] the open topology of the tubular phase has been acknowledged only as a result of pinning and defects, while the closed topology (laminar) being accepted as the only thermodynamic equilibrium state and little attention was devoted to pinning or shape. My research has focused on the effects of sample shape and applied current in respects to these structures in the intermediate state with hopes to conclusively state that the tubular structure is indeed another thermodynamic equilibrium.

CHAPTER II. EXPERIMENTAL SETUP

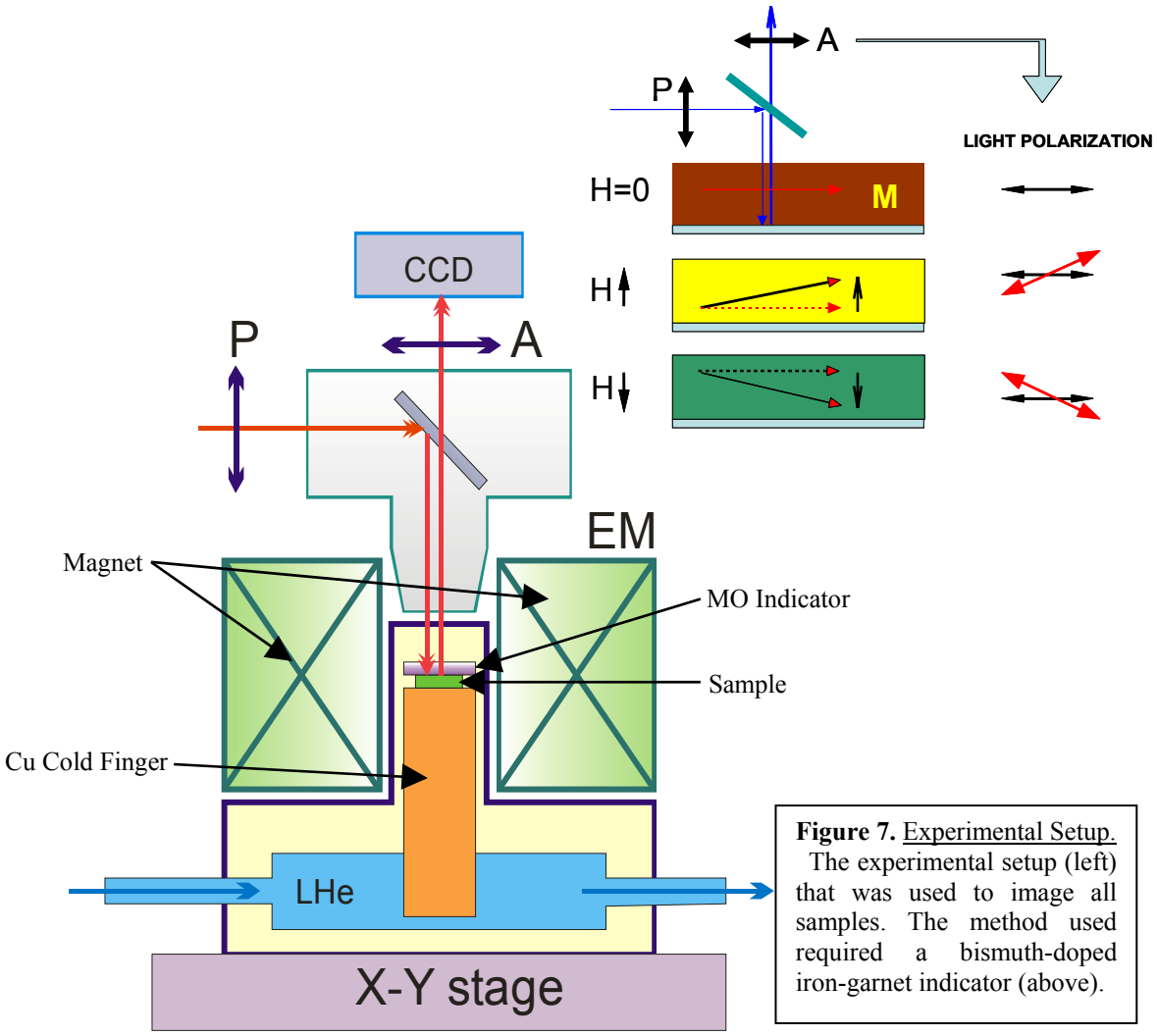

Figure 7. Experimental Setup. The experimental setup (left) that was used to image all samples. The method used required a bismuth-doped iron-garnet indicator (above).

In all of the following experiments, the equipment shown in Figure 7 was used to image the magnetic field. This setup consists of a flow-type liquid ^{4}He cryostat that sits upon an adjustable X-Y stage. The liquid ^{4}He is transferred from a transport dewer through a transfer line designed for this system. The helium then flows through a heat exchanger which wraps around the base of a copper cold finger, a round stage 10 mm in diameter. The sample sits upon the cold finger. A bismuth-doped iron-garnet indicator[22] is placed flush on top of

the sample. This indicator is a multi-layered structure with in-plane magnetization and a mirrored bottom. The cold finger, sample and indicator are located inside a sealed vacuum chamber with a glass lens to allow light through. Polarized light passes through the indicator, reflects off the mirrored bottom and then passed through an adjustable analyzer rotated roughly 90^{o} with respect to the original polarization. A CCD camera displays the resulting real-time images. An external field is applied using a solenoid magnet with a coil constant that is approximately 255 Oe/A. Inside the cryostat are two thermometers, a heater and contact leads which are available to pass current through the sample. One thermometer is reads the temperature on the heat exchanger. The second thermometer is placed toward the top of the copper cold finger to get an accurate reading of the sample temperature. The heater is also in this area to effectively heat the sample.

Imaging of the magnetic field in the surface of a sample was available through the iron-garnet indicator's in-plane magnetization. As shown in Figure 7, an external field in the z-direction will polarize the magnetic moment inside the indicator correspondingly. According to the Faraday effect, polarized light that passes through a dielectric material magnetized in the direction of propagation will rotate proportionally to the intensity of the z-component of the magnetization (Figure 6). Once the reflected, rotated light passes through the analyzer, the resulting intensity is directly proportional to the z-component of the magnetization of the indicator. Because I place the indicator directly on the surface of our sample, any z-component of the indicator's magnetization comes directly from the surface of the sample. Resulting images have differing colors associated with opposing sample magnetizations. As an example, Figure 8 shows the imaging of a credit card barcode. In general, the sample images of superconducting Pb contain green regions associated with the

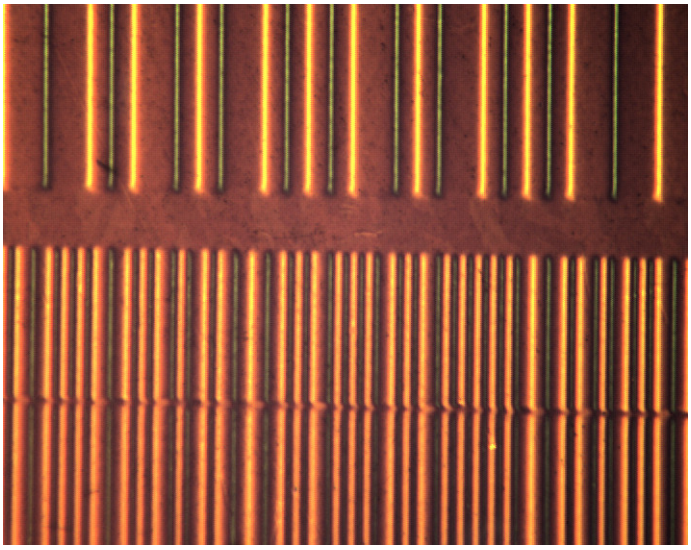

Figure 8. MO Imaging. This image shows the magnetization at the surface of a credit card, revealing the barcode. The green and orange colors represent opposing magnetization directions.

normal state and dark, almost black, regions associated with the superconducting state. In some experiments domains were observed in the indicator. These domains denote areas in the indicator where the in-plane magnetization points in two different directions. The opposing domain magnetizations create small z-components of the magnetization in opposing directions. These small z-components, in turn, create two slightly different domain colors. In all cases, these domains are purely cosmetic and have no effect on the experiments.

Overall, this experimental setup can image the magnetic field at the surface of bulk samples with a spatial resolution of 3 μm to 10 μm. The temperature range achievable is 3.8 K to 300 K. Temperatures below 4.8 K are reached by pumping directly on the helium and adjusting the needle valve of the transfer line. The applied magnetic field can be increased to 1800 Oe with <0.5 Oe sensitivity, and a current of almost 2 A can be passed through the sample. All imaging is saved and analyzed through the computer program

QCapture Pro. Also, I recorded real-time video of the experiments on a VCR. The sample temperature, exchange temperature and applied field are all recorded using LabVIEW.

When using this experimental setup, some technical details must be considered. First, the indicator must be both flush with the surface of the sample and perpendicular to the incoming light to image the magnetization. The indicator's magnetization is only affected by external magnetization over a very small distance[5] (roughly 3 μm), which is why there is a need for flush contact with the sample. Also, the indicator must be perpendicular to the incoming light to reflect the light directly back to the CCD. This means that all samples are required to have a flat upper surface oriented parallel to the surface of the copper stage. This restraint will be explored in detail in the next chapter. Also, the light intensity, image color and contrast were constantly monitored for ideal imaging. Additionally, when working with a cryostat it is important ensure that the temperature is consistent and that the temperature reading is an accurate portrayal of the sample temperature. Temperature control will also be discussed in the next chapter.

CHAPTER III. EXPERIMENTS

1. Sample Preparation

All the experiments that I will discuss through the course of this thesis have been performed on Pb samples of different size, shape and quality. I have used three different methods in sample preparation thus far. The first experiments were performed on samples of differing shapes (slabs, cones and hemispheres) that were created using molds. Oxygen-free copper molds were milled to specification by the metals development group of Ames Laboratory. These molds were placed on a hot plate inside an inert gas atmosphere. Chunks of 99.999% pure Pb were placed inside the molds and then melted. Problems arose when the surface tension of the liquid Pb caused an unwanted surface bubbling effect. Because direct indicator contact is required for proper imaging of the surface magnetization, polished steel plates were placed directly on top of the molten Pb to create a flat sample surface. In some cases, the solidifying Pb condensed to a size such that the surface of the sample was below the lip of the copper mold. In these cases, the sample was removed from the original mold and placed in a second mold with a shorter lip. Using this molding method, many samples of different sizes were created.

Some of the best imaging was achieved using single-crystal samples. Pb disc samples were purchased from three companies, MaTeck GmbH (MT), Metal Crystals and Oxides Ltd. (MCO) and Goodfellow. The crystals from both MCO and Goodfellow were found to have very high pinning, while the MT crystals were clean (of minimal pinning) samples and have helped set a basis for the research that followed. Because of the high quality disc-shaped samples we received from MaTeck, a single crystal hemisphere was purchased. Imaging of this hemisphere has been difficult and will be discussed in the next section.

Most recently, I observed the intermediate state in Pb strips with an applied current. Samples for this work were cut from larger foils of differing thicknesses that were purchased from two companies: Alfa Aesar and Goodfellow. Similar to the Pb disc crystals, only one of these companies — Alfa Aesar — provided samples with minimal pinning. The amount of pinning in the Goodfellow strips can be seen in papers by Jeudy *et al*.[23-28]. For my research, I cut the Pb strips with a straight razor blade into the sizes needed. Cutting the strips in this fashion introduced edge defects that acted as places of first penetration. After being cut to the desired shape, each sample was placed on the cold finger and connected to current leads that wound through the cryostat. The leads were attached using either solder or, more commonly, by silver paint. The silver paint provided good connections without heating the ends of the Pb samples. Alfa Aesar strips of thicknesses 0.1 mm, 0.25 mm and 0.5 mm were studied.

All of the samples measured were mounted onto the cryostat's copper cold finger using Apriezone-N low-temperature grease. In the case of samples in a mold, grease was used between the mold and the stage. Grease was only used between the sample and the mold if the sample had come free of the mold. The crystal slabs were placed directly on top of the cold finger with a grease thermal connection. The Pb strips were placed on the cold finger in a similar manner. Current contacts that were connected using silver paint covered the entire end of the sample to allow uniform current flow.

2. Experiments on Samples of Different Shapes

The first experiments performed were done to answer the question, "How is the intermediate state affected by bulk sample geometry?" To answer this, three basic geometries were measured: slab, cone and hemisphere. The magnetism of samples with shapes similar to those I will discuss was looked at by Provost *et al*.[29]. The measurements that I will discuss show that geometry played a large role in the flux structure created either through the sample's geometric barrier[30,31], or by affecting the energy required to move the magnetic flux.

i. Slabs

The first experiments conducted when looking at different shaped samples were performed on Pb slabs. The term "slab" is used here to describe a geometry consisting of two large, parallel surfaces that are perpendicular to the applied field. The first of these samples had a square face, and were molded according to the description in the Sample Preparation section. The preliminary results show two distinct flux structures after approaching the same point by following two different paths in the H-T phase diagram (Figure 4). By ZFC the sample to a fixed temperature of approximately 4.8 K and increasing the applied magnetic field, the intermediate state was reached and the magnetic flux entered the sample as tubes. After the applied field was large enough to saturate the sample and enter the normal state, the field was decreased, re-entering the intermediate state. Once the intermediate state threshold was crossed, superconducting lines appeared. These lines oriented themselves in such a way that, as the flux density decreased, the Landau laminar[13] structure formed. This structure's density remained roughly constant across the sample and thinned out as the applied field was

decreased. Imaging of the square-faced slabs proved to be unclear while the samples themselves were still highly pinned. The imaging of the crystal discs proved to be of much better clarity.

A thorough inspection of the magnetic structure formation in a Pb slab was available through measurements of Pb disc crystals ordered from MaTeck GmbH (referred to as MT from here). There were two crystals, each 5 mm in diameter and 1 mm thick. The difference between the crystals is the crystal orientation: 111 and 100. There was no difference found in the magnetic patterns, however. Clear imaging of the intermediate state of the Pb crystal disc MT 111 is shown in Figure 9 and Figure 14. Figure 9 shows the increase of an applied field while Figure 14 shows the decrease. All images were taken at 6 K. Similar to what was found in the Pb square slab, at low fields (93 Oe) the sample is nearly completely superconducting. Remember that dark regions are superconducting, while colored areas are normal. The color surrounding the sample in the images is the indicator's reaction to the applied field. The only field that is entering the sample is at the edge. This edge penetration is the result of the magnetic field wrapping around the corners at the edges and is looked at more thoroughly in Figure 10. At the slightly higher field of 109 Oe, the first magnetic flux enters the sample via jets of flux tubes. This fast flux flow occurs at a terminal length of the original finger-like penetration. All tubes that are created are pushed to the center of the sample by the Lorentz force created by the supercurrents inside the Meissner state. Subsequent tubes are then forced to the center, building the central tubular formation and decreasing the size of the diamagnetic band. This structure is evident in the images corresponding to 109 Oe, 115 Oe and 168 Oe. At 168 Oe, the central tubular structure grows to a size that starts to decrease the length of the edge structure, and at 190 Oe, the edge flux is nearly gone. This decrease in

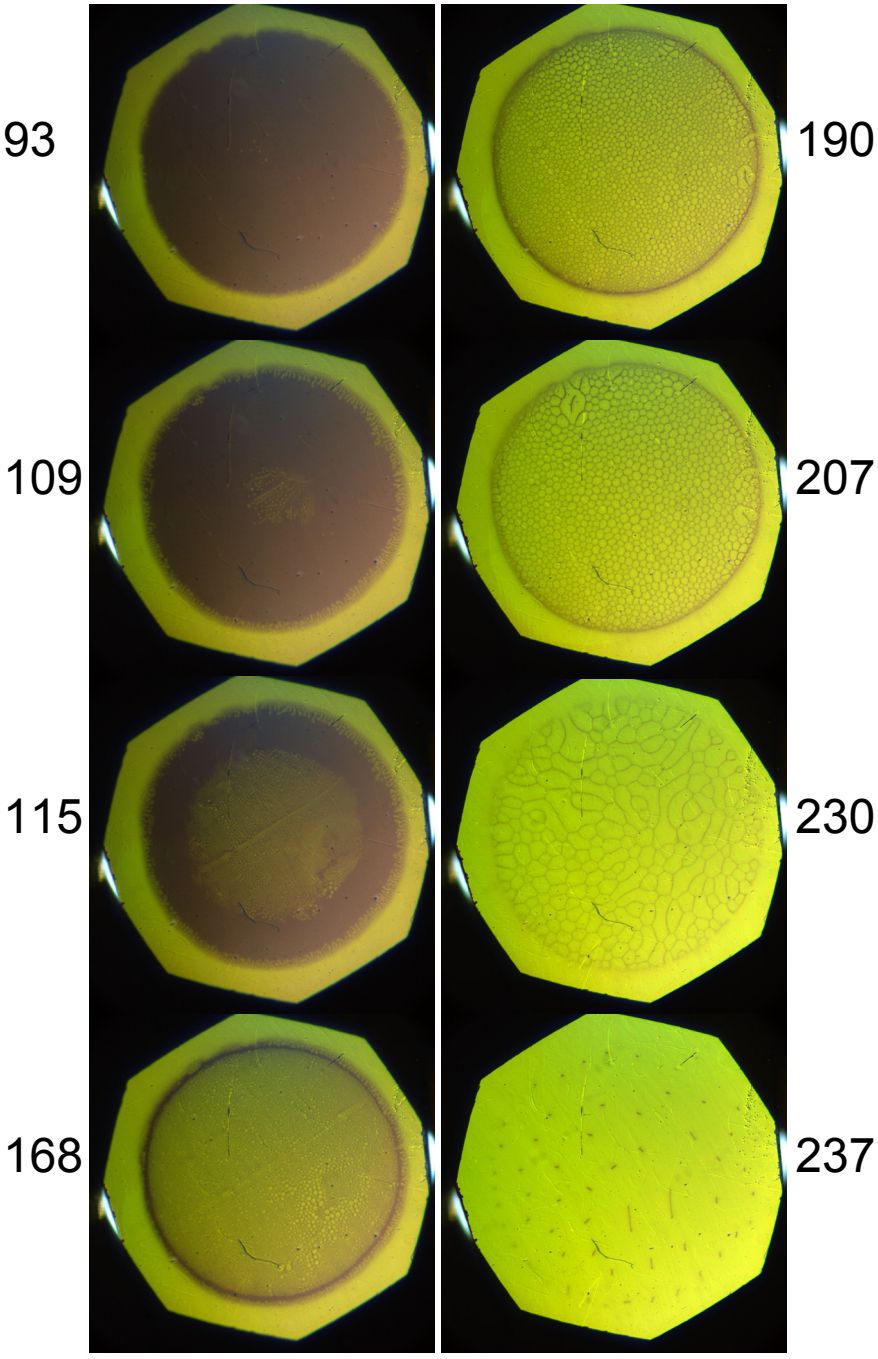

Figure 9. MT 111 Increasing Applied Field. Each number is the associated applied field (Oe). This set of images shows the flux structure of the intermediate state after ZFC, and crossing the SI interface.

edge flux maintains the diamagnetic band (and the supercurrent) in the sample. By 207 Oe applied field, the central flux structure has reached the edge of the sample and the internal flux is at a high enough density that the smaller tubes originally created have merged and created larger tubes. The structure here and in the 190 Oe image have a high resemblance to that of two-dimensional dried soap foam. This structure and its relationship to foam physics

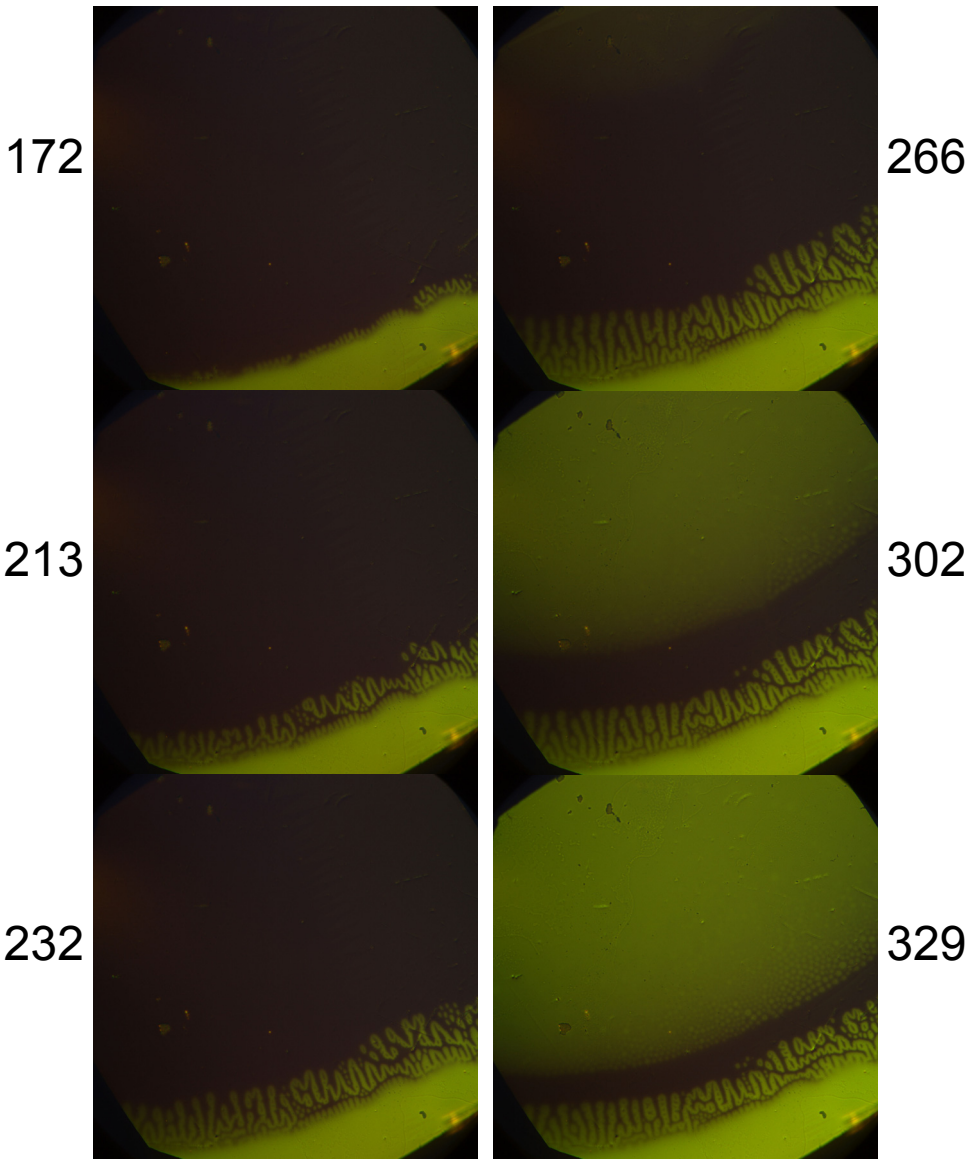

Figure 10. Flux Entrance. A close-up look at how the magnetic flux enters the sample. Each number is the associated magnetic field (Oe).

is discussed in the Discussion chapter. As the sample approaches saturation, the foam structure dissipates to a pseudo-laminar structure (230 Oe). At 237 Oe the flux density is so high that all that is left of the Meissner state is superconducting dots representative of superconducting threads passing through the depth of the sample. These threads occurred in all of the samples measured and always align in the periodic manner shown in Figure 9. Note that the statement that these are superconducting threads is an extrapolation of the surface magnetization and it is also possible that these dots are superconducting pockets located in the sample surface only.

Now, before examining the laminar structure that results from crossing the NI interface, we will take a closer look at the tubular structure and its manifestation. Figure 10 contains close-up imaging of the Pb MT 111 crystal disc. Shown is the formation of first penetration along with the reaction to the increasing central tubular structure. As can be seen, the flux penetration at the edge forms a complex finger-like structure that reaches a maximum length (232 Oe) before the first flux tubes nucleate. The central tubular structure then forms and continues to grow, diminishing the diamagnetic band and, as stated before,

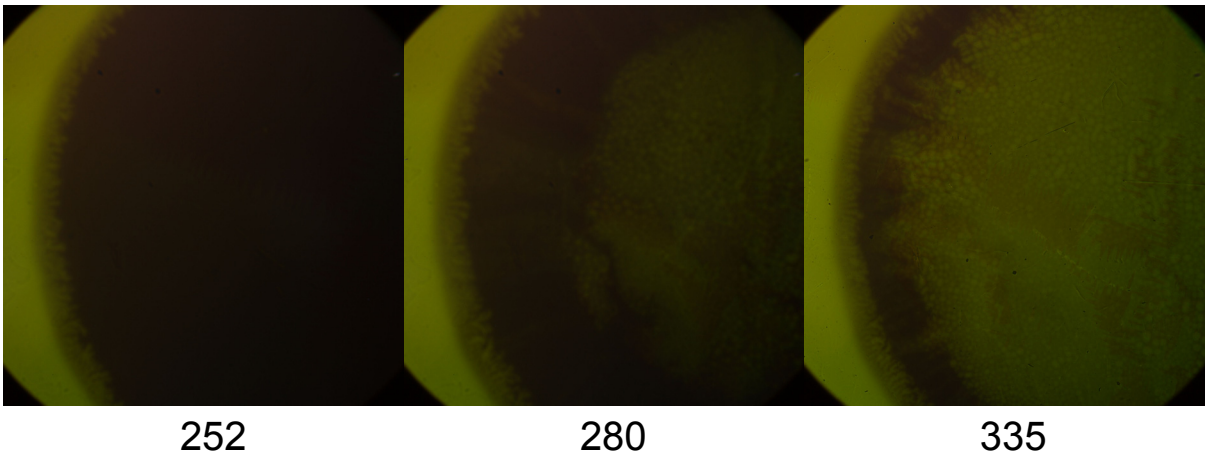

Figure 11. Flux Tube Jets. The images shown depict the motion of the flux tubes under the Lorentz force.

pushing the edge penetration back. The shrinking of the finger-like structure is evident when comparing the 329 Oe image with the 232 Oe image. This effect is further discussed in the Discussion chapter.

The process of flux tube nucleation is an interesting one. While Figure 11 shows a close-up of flux tube jets, a simply drawn explanation of the event can be seen in Figure 12. The figure depicts the cross-section one-half of the sample. The magnetic field is applied toward the bottom of the sample and as the field intensity increases, there is slight penetration of field at the sample corners. One can understand this penetration if one imagines that the applied field wraps around the sample as depicted in Figure 2 of the Introduction. This flux entrance at the corners is the finger-like structure depicted in

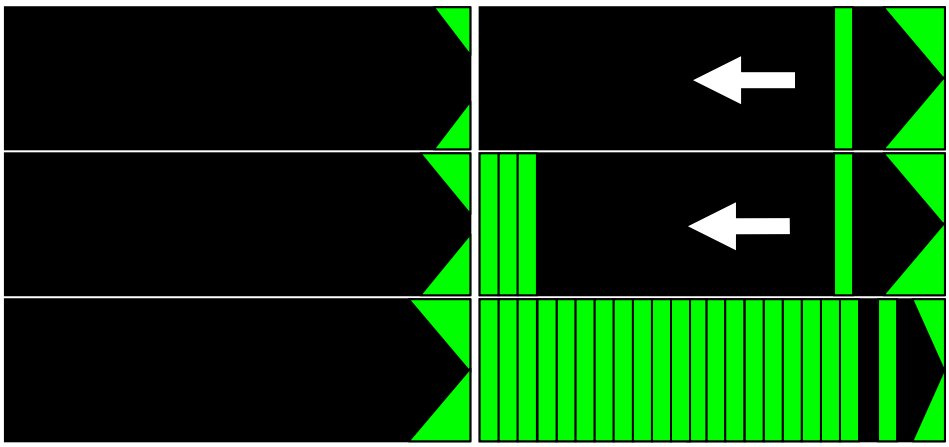

Figure 12. Edge Penetration and Flux Tube Formation. This sequence of images shows how the edge penetration grows and nucleates tubes.

Figure 10. And, as the applied field is increased, the size and length of the edge structure increases. This continues until the magnetic field at the bottom corner of the sample reaches the magnetic field at the top corner. At this point, a flux tube is created (depicted in the upper right image). The Lorentz force then drives the flux tube to the center of the sample (left portion of all images) and continues to drive additional tubes, slowly stacking flux tubes

from the center outward. And, as shown in Figure 12, after the flux tubes start to reach the outer sample edge, the field penetration at the corner doesn't need to be at as sharp of an angle as it was, and the field "retreats" back. This flux tube nucleation is the core idea behind the geometric barrier. Due to the sample shape, there exists a distribution of supercurrents that delay the penetration of magnetic flux into the sample center. The geometric barrier is explored thoroughly by Zeldov *et al*.[44].

The flux entrance and "jetting" motion is a result of the Lorentz force: $\vec{F}_L = I \cdot \vec{l} \times \vec{B}$, where, $\vec{F}_L$ is the Lorentz force vector, I is the magnitude of the current, $\vec{l}$ is the length vector and $\vec{B}$ is the vector associated with the magnetic field. Due to the pure diamagnetism of the Meissner state, any small applied field is counteracted inside a superconducting material by a supercurrent. In cylindrical coordinates, if the applied field has a direction of $\hat{z}$, then the diamagnetism in the sample will oppose this by creating a supercurrent, I, in the $-\hat{\phi}$ direction (corresponding to $\vec{l}$). Now, once there is a flux tube created, that flux tube will contain field that is in the same direction as the applied field, i.e. $\hat{z}$. The resulting force on that flux tube, according to the Lorentz force, is in the $-\hat{r}$ direction and the tube is pushed to the center of the sample.

It is possible here to pose the question, "Why do the flux tubes stack at all?" This is a valid question because, as was stated in the Introduction, the wall energy of each tube is positive. While this question has a straight forward answer, it is not immediately obvious why the tubes wouldn't merge immediately, minimizing the wall energy. The answer lies in the fact that each tube has an associated shielding current that flows around it in the conventional way ($+\hat{\phi}$). When a second tube approaches the first and gets close enough, the

currents associated with each tube cancel. This stops motion and creates a minimum distance between flux tubes and as more tubes are forced in, the tube structure enters an equilibrium that is constantly changing with the changing applied field.

Figure 13 depicts a magnified image of the MT 111 Pb crystal and provides an examination of the magnetic flux tubes. The sample had been ZFC and brought to the intermediate state by increasing the applied field. Before the sample was brought to saturation, the applied field was decreased in each subsequent photo. There are two important aspects of the structure here. The first is evident in all three images: the "holes" inside a majority of the tubes. These "holes" are actually what Landau referred to as "branching[13]." Although Landau only postulated this effect in the laminar structure, branching in a flux tube should also be expected as this effect is caused by the magnetic flux deviating from the center of the tube as it reaches the sample surface in order to wrap around and close the field loop. The second aspect to consider is the formation of the flux tubes that are circled in white in the third image. These tubes have a unique shape that was formed by the decreasing applied field combined with the relative isolation from surrounding flux. What makes this formation important is the direct physical relation to the prediction for flux domain boundary

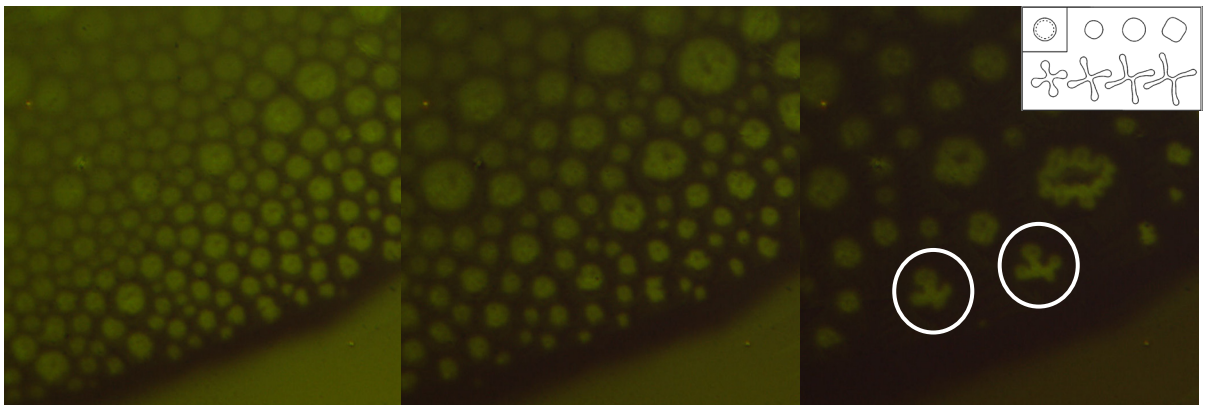

Figure 13. Flux Tube Magnification. The images show flux tubes in a decreasing (left to right) applied field. The insert is the prediction of flux domain boundary motion made by the current loop model[32].

motion, shown in the insert in the upper right, which is made by the current loop model proposed by Goldstein, Jackson and Dorsey[32]. Both this relationship and the relationship of dense flux domain structure to the physics of foams is discussed in the Discussion chapter.

While there is rich physics involved in the tubular structure, a majority of work has been performed on the Landau laminar structure. Figure 14 shows the MT 111 Pb crystal disc after saturation and in a decreasing applied field. This crystal is the same as was imaged in Figure 9. As the field is decreased from the normal state, the intermediate state appears with the formation of superconducting lines at 226 Oe. The superconducting lines enter the sample seemingly at random, but are most likely affected by any small defects at the edge of the sample. The superconducting lines' original orientation will shape the laminar structure formed at lower fields. This is evident in Figure 14 at 212 Oe. While the structure looks different, there still remains the general superconducting structure from the previous image. This trend continues at lower fields, but is less noticeable as edge defects play a larger roll in the motion of flux as it exits. At 190 Oe, flux branching has really started to become prevalent and is a uniform attribute at both 150 and 128 Oe. Also, at 190 Oe, the edge defects become evident. There are two major edge defects on the left had side of the crystal. These are the points where the laminar structure is nearly perpendicular to the sample edge and have been marked with white circles. Defects like these are points where it is easier for magnetic flux to both enter and leave the sample. In Figure 9, one of these edge defects can be seen affecting the tubular structure at higher fields (207 Oe).

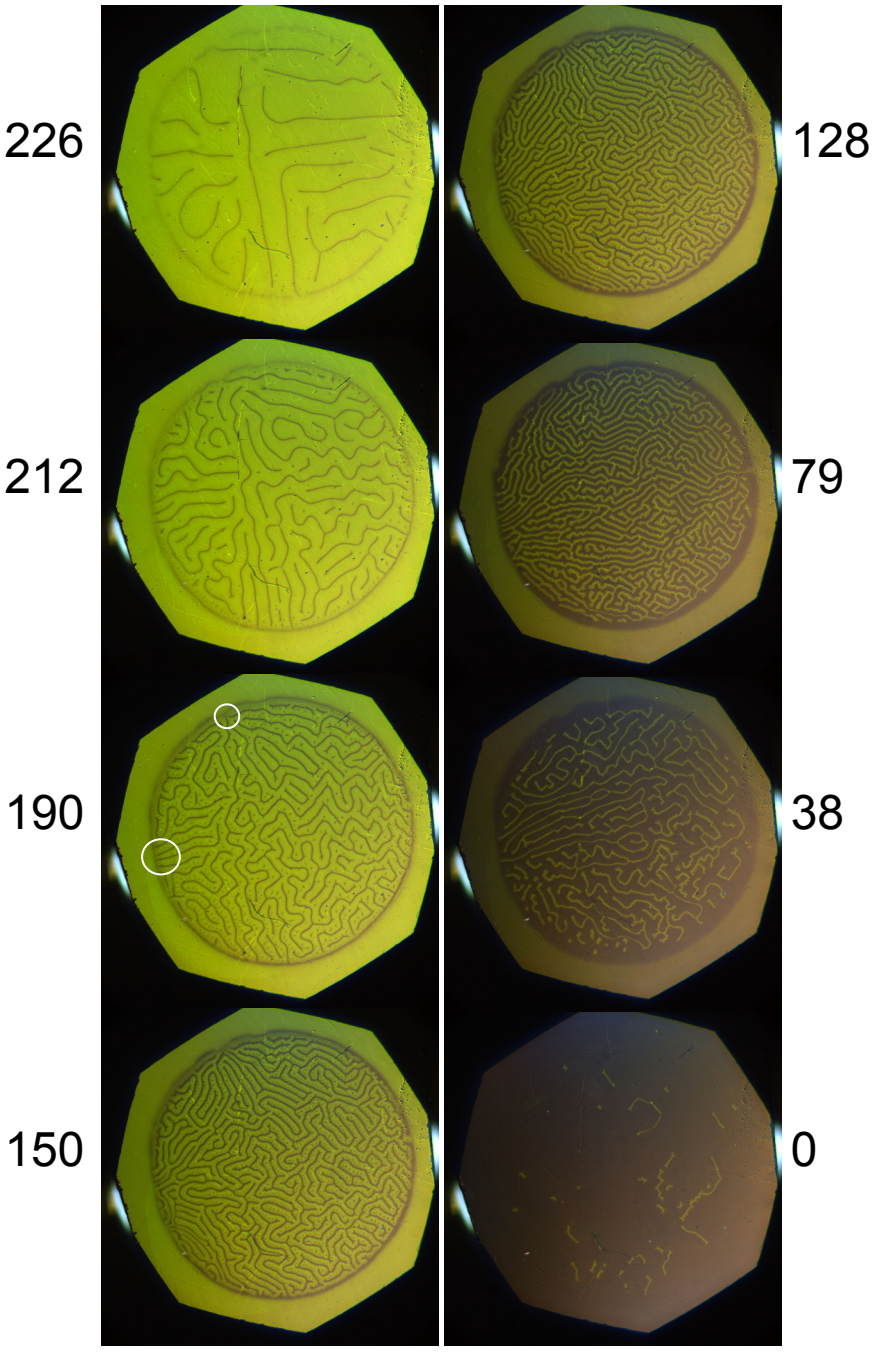

Figure 14. MT 111 Decreasing Applied Field. Each number is the associated applied field (Oe). This set of images shows the flux structure of the intermediate state after saturation, and crossing the NI interface. The white circles mark edge defects.

While at lower fields, the laminar structure pulls away from the edge — allowing for a small diamagnetic barrier — in general the structure stays uniform. The flux only "thins." At 128 Oe, the structure becomes so thin that the branching effect results in a corrugation[42,43] of the laminar edges. This is counterintuitive due to the positive wall energy. However, this effect is short lived, and by 38 Oe the majority of the laminar flux is smooth-edged. Also at 38 Oe there are a few stand alone flux tubes located at the bottom of the sample. This is the laminar structure breaking into tubes and is a trend in every sample that was measured. The occurrence raises the question, "By what mechanism does magnetic flux leave a sample?" The last image at 0 Oe shows the amount of pinned flux left in the sample. The amount of structure left is very little, leading to the conclusion that this crystal contained only weak pinning.

Earlier, in the Sample Preparation section, there was mention of a set of Pb crystals ordered from a second company. We purchased two Pb crystals from Metal Crystals and Oxides Ltd. (MCO) for observation of the intermediate state. Unfortunately, these crystals had very high pinning and, therefore, were basically unusable. Figure 15 depicts the extent of the pinning in these crystals. For this image, I applied magnetic field (not to saturation) and then turned off the field. The green in the center of the image is trapped magnetic flux from this first step. I then flipped the direction of the applied field from the solenoid, and the magnetic field was increased slowly until anti-flux (yellow) was visible. What should occur in a type-I superconductor is the magnetic flux should leave immediately once the magnet is turned off, and if any flux is pinned the application of anti-flux should cancel and dispel any remnant field. Obviously the pinning in the MCO crystals was much too high to gather any usable data.

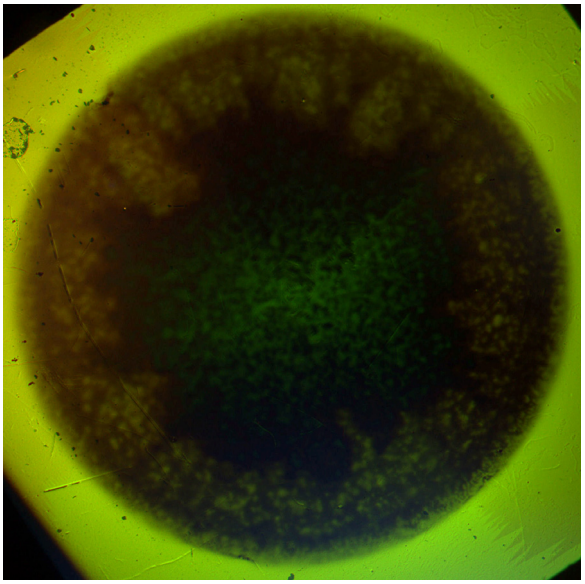

Figure 15. MCO Crystal. The image shows the intense pinning in the sample.

Finally, the last slab-type sample that I imaged was the Pb strip. Shown in Figure 16 is a strip with dimensions 9.30 mm x 1.85 mm x 0.48 mm that was cut from a larger film produced by Alfa Aesar. The left and right columns have corresponding applied fields listed to the left of each set of images. The sample was first ZFC. Then an external field was applied to the sample. The field was increased to saturation (left column, top to bottom), and then decreased (right column, bottom to top). While, in general, the sample behaves just as the MT crystal behaved — with flux tubes upon flux entry and laminar structure with flux exit — there are a few comments that should be made. First, the sample has edge defects as were described earlier. These defects are evident in the 200 Oe and 250 Oe images with flux entry as there is only flux penetration from the top edge and this penetration is pseudo-dendritic. This one-sided penetration is a consequence of the crude way in which the sample was cut (with a razor blade). The second comment is that the sample is not a single crystal. The sample does contain some pinning. This pinning is most evident at the 350 Oe flux entry image. There is a mixture of both flux tubes and laminar structure. This combined structure is

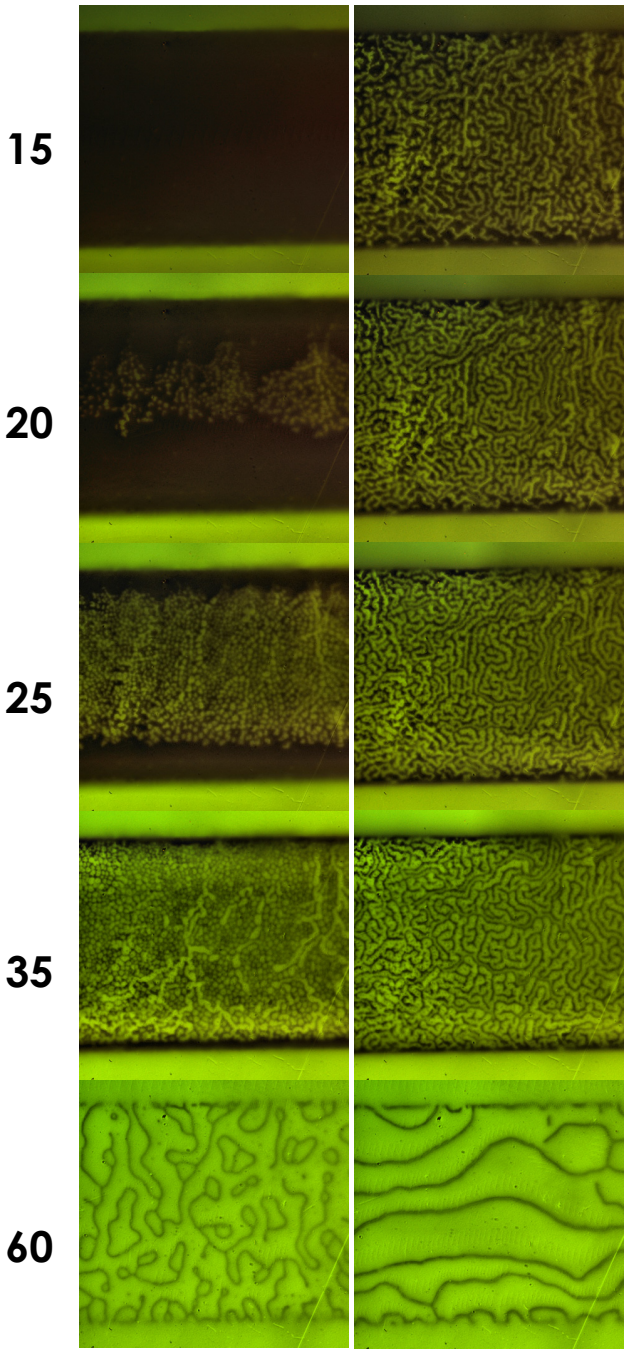

Figure 16. Pb Strip. The left column shows flux entry (top to bottom) and the right column shows flux exit (bottom to top). Each image is at the field listed to the left in Oe.

due to a flux tube coming into contact with a strong pinning point. This concept will be examined further in the Discussion chapter. Finally, in the 150 Oe image of flux exit (right column) there again can be seen single flux tubes appearing during flux exit.

ii. Cones

Working with samples that are not flat has been a challenge for good imaging. In most cases, the surface was not uniform, or it had solidified below the rim of the mold. As a result, most images were blurry as the indicator was not flush with the sample surface. Also, many of the cone-shape samples had a very unique problem that arose from the machining of their molds. Machining the cone molds was a process that required the use of increasingly smaller drill bits. Because there is not an easy way of making a continuous slope, many molds had minute "steps" along the inside. These steps affected the sample in two major ways: the sample itself had steps and during the cooling of the sample and mold, the mold constriction provided a non-uniform stress. Figure 18 and Figure 19 show some of the best imaging that we were able to achieve using the method of molding.

Both the cone-shape and hemisphere-shape have been shown to have no geometric barrier[20]. This plays a very large role in the magnetic flux structure. As will be seen, the structure takes similar shape to what was observed in slab samples, but has subtle differences based on the sample shape. Figure 18 shows a cone-shape sample with a 2.5 mm diameter as the applied field (in Oe) is slowly increased, while Figure 19 shows the same sample with a decreasing applied field (in Oe) after saturation. At a first glance, there are many obvious differences between the cone and the Pb disc that was discussed earlier. While these images show the flux entry, there is not a clear tubular phase as there was in the disc. There appears

to be a mixture of both the tubular and laminar state. This combination is due to pinning. Also, the flux structure doesn't jet into the center as the flux did for the disc. It simply moves in toward the sample center as the applied field is increased.

I'd first like to address the blurry areas of these images. They should be ignored when examining the details of the flux structure. These areas are a direct result of the molding process. Figure 17 is an image of the bare sample surface. It is not a perfect mold nor does it have a perfectly flat surface. The red-brown color that surrounds the cone sample is the copper mold it was made in. The Pb itself is cracked and, in places around the edge, has spilled over onto the mold. The parts of the Pb that has spilled over can be seen in the magnetic images as darker flux-filled regions surrounding the central cone. These spillovers have little to no effect on the general flux structure of the sample. The interesting areas here are the areas that have the greatest visual affect on the structure, as they are the dark areas on the sample surface. Because the light used to image the surface is reflected polarized light

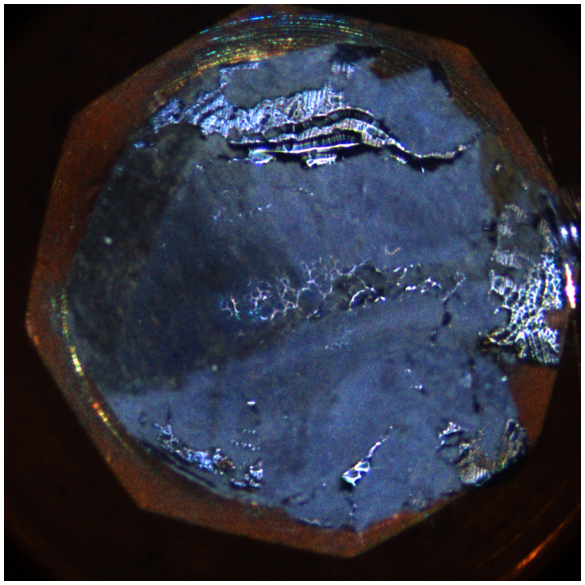

Figure 17. Cone Sample Bare Surface.

that passes through an analyzer, the difference in brightness on the surface represents the surface contours. The brighter areas are the flattest, most perpendicular to the incoming light, as they reflect the most. The dark areas are, in this case, depressions in the sample surface and, therefore, regions where the indicator can't sit flush. This results in the blurry areas that appear in the magnetic imaging. One would expect the shiny area at the top of the sample to have a major effect on the flux formation imaging. However, this is not the case. This is an area that is still flat, but did not oxidize during the molding of the sample and simply reflects light more than the oxidized regions surrounding it. The dark "ridges" do play a small role, and if one looks closely at the magnetic imaging, can see small blurry stripes that align perfectly with the dark ridges. The last, and probably most evident, result one can draw from Figure 17, is that there is pinning throughout the sample.

With a better understanding of the surface defects of the sample, the magnetic flux structure can be studied while the defect areas can be ignored. In the 199 Oe image in Figure 18, the flux entrance does not seem to differ much from that of the Pb disc. There is a finger-like structure that has penetrated the edge. With close inspection, though, there are quite a few flux tubes interspersed throughout this first flux penetration. While a similar phenomenon can be observed in the flux penetration of the disc (Figure 10), the question of why these tubes do not move immediately to the center arises. This lack of motion can be explained by a required increase in tube length as the tube moves toward the sample center. This slow entrance is explored in more detail later in the Discussion chapter. The overall flux structure gets more confusing as the applied field increases. Less than or equal to an applied field of 359 Oe there is still no magnetic flux in the center of the sample, and the overall structure seems to be a mixture of both the laminar and tubular phases. At the higher fields

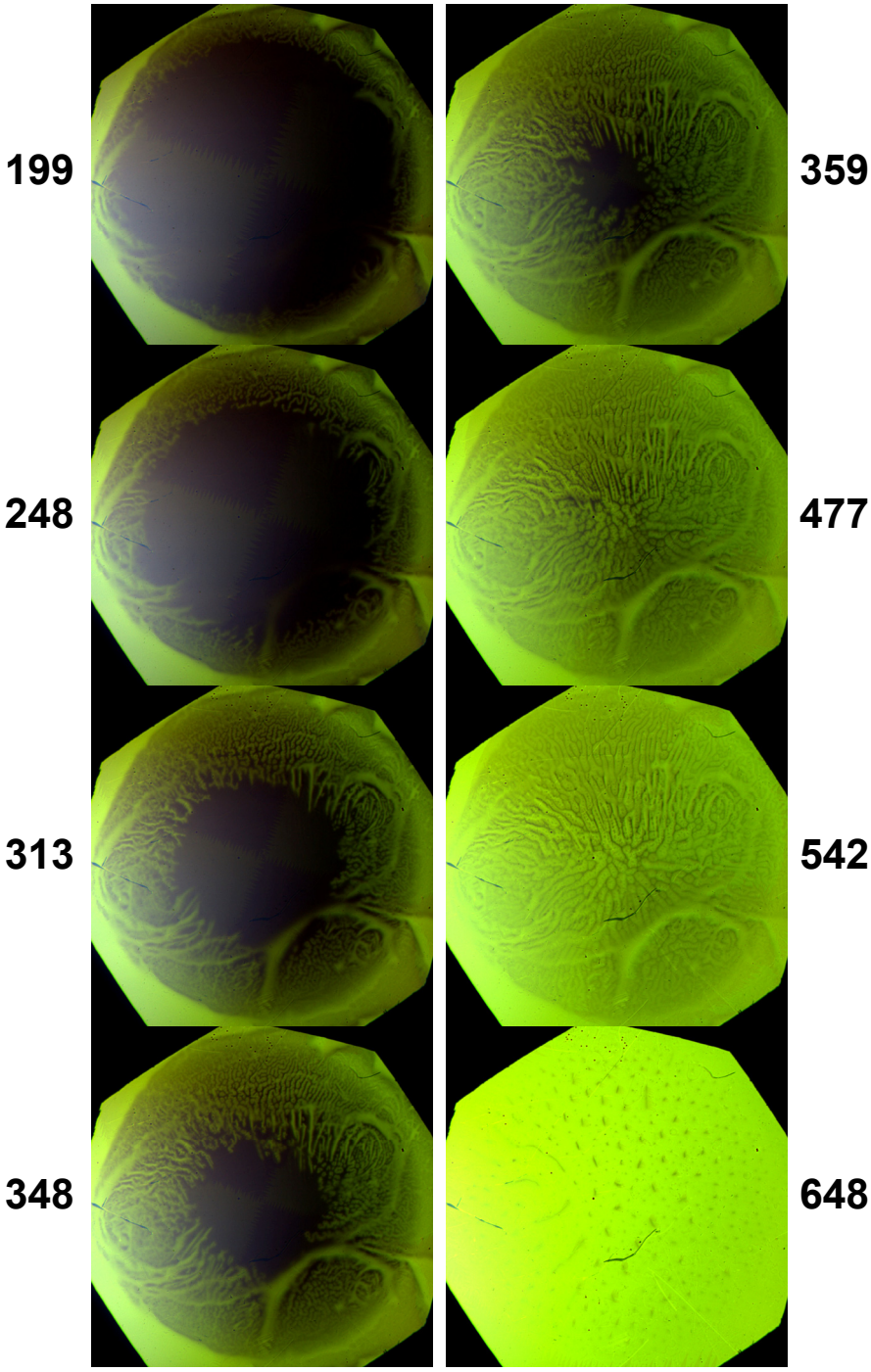

Figure 18. Cone with Flux Entry. The series of images shows an increase in applied magnetic field (Oe) from a ZFC sample.

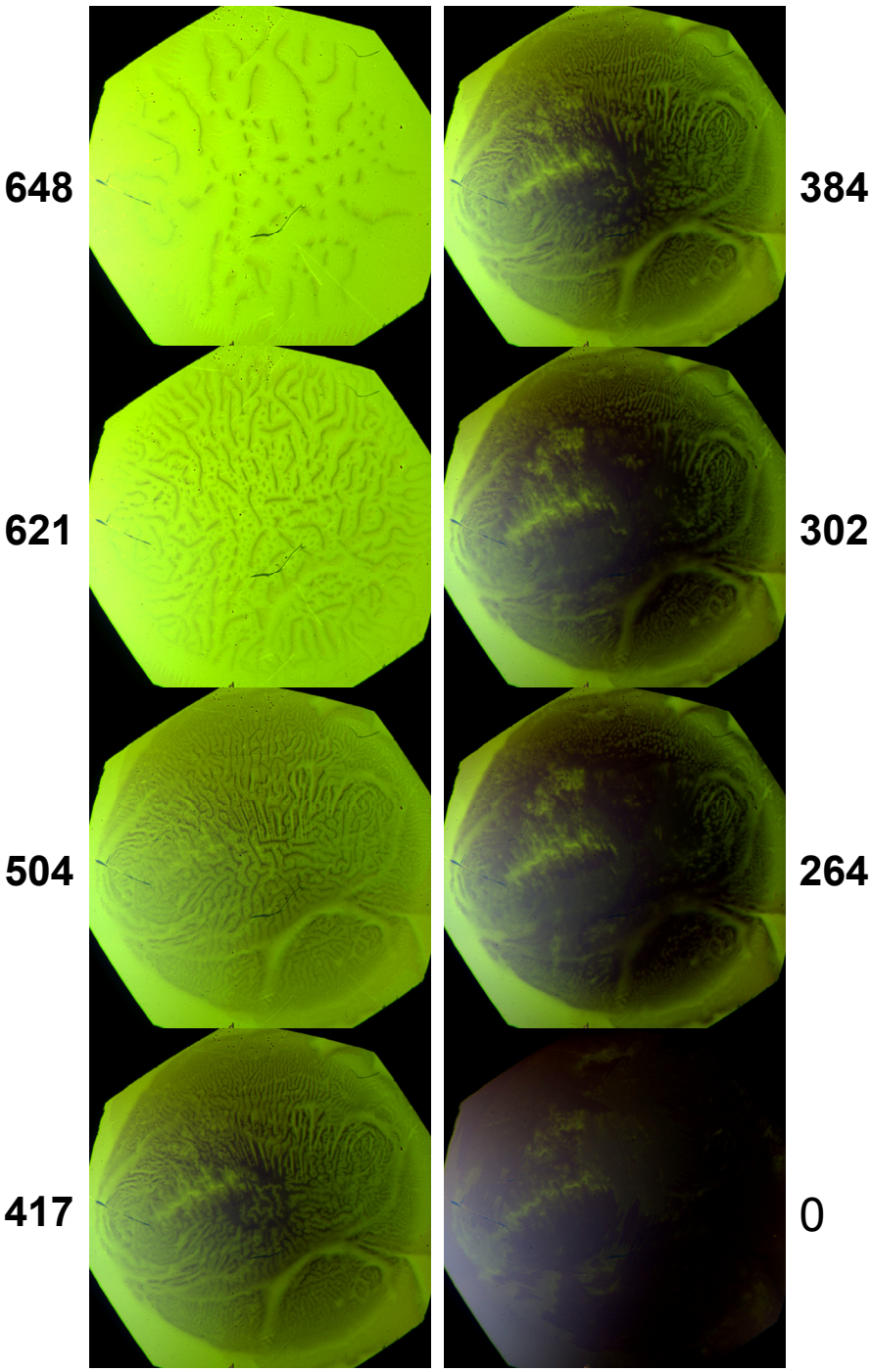

Figure 19. Cone with Flux Exit. The series of images shows a decrease in the applied field (Oe) from saturation.

(542 Oe and 648 Oe), the sample behaves/saturates in an expected way. After saturation, when the field is decreased (Figure 19), the flux structure is similar to the Pb disc at the higher fields. At 417 Oe and below, however, the field structure mirrors that which occurred upon flux entry (Figure 18). The magnetic field leaves the sample such that there is a superconducting center while continuing to keep both laminar and tubular phases throughout. For this sample, two questions arise: why does the flux move in and out leaving a superconducting center; and what (if any) is the preferred intermediate state structure? While the second of these questions is still under dispute, the first can be answered by looking at the energy contributions to the system. Both questions will be discussed in the Discussion chapter.

iii. Hemispheres

Just as with the Pb cone, imaging a Pb hemisphere was a challenge. Many of the same surface problems with the cones were found in the hemispheres as well. The hemispheres did not have the issue of non-uniform stress because the mold milling process could be performed with a single round-tip drill bit. There was a separate problem with the hemisphere samples that came loose from their mold. Because the sample was no longer fixed to the copper mold, it was important to ensure the sample and the cryostat cold finger had a good thermal connection. This was achieved by applying a small amount of Apriezone-N grease between the sample and the mold (there is always grease between the mold and the cold finger). The problem arose while the sample chamber was vacuumed. Any air bubbles trapped in the grease beneath the sample tried to escape. This motion of the grease caused the sample to tilt, ruining any attempt at imaging. This became a big problem when we attempted

to image the MT Pb crystal hemisphere (Figure 22). Our solution to this was to a drill hole that passed from the bottom of the sample cavity to the side of the mold. This addition allowed the air in the grease to escape from directly beneath the sample, keeping the sample surface perpendicular to the polarized light.

Barring these obstacles, I was able to acheive good imaging of a few hemispheres. Figure 20 and Figure 21 are two different Pb hemispheres that were molded and successfully measured. Each of these two sets of images show an increase in applied field (left column) to saturation followed by a decreasing field (right column). Both of these samples had large pinning. In Figure 20, the indicator had slipped to the left so that at the right of all images both the sample and the mold are visible. In this figure, however, you see very similar attributes as those in the Pb cones. There is a slow flux entry, but the field enters the center of the sample at a smaller field than the cone sample. This central flux structure is much more like the tubular phase that appears in the crystal disc. As the sample approaches saturation (the bottom left image), a few flux tubes are still mixed in the flux structure. After saturation (right column), the Landau laminar structure is apparent. Almost immediately, as the flux dissipates, the laminar structure breaks into tubes. The tubes are almost the only structure that is left in the third image, and the last image shows that there was some pinned flux.

The sample in Figure 21 depicts a flux structure that is harder to analyze, as there was a lot of pinning in this sample. Throughout most of the images, there is again (as there was in the cone) a mixture of the tubular and laminar structures. I would like to bring attention to the first image on flux entry (189 Oe) and the last two images on flux exit (183 Oe and 148 Oe). In the first image, all the flux present entered at one large edge defect. This point is circled in

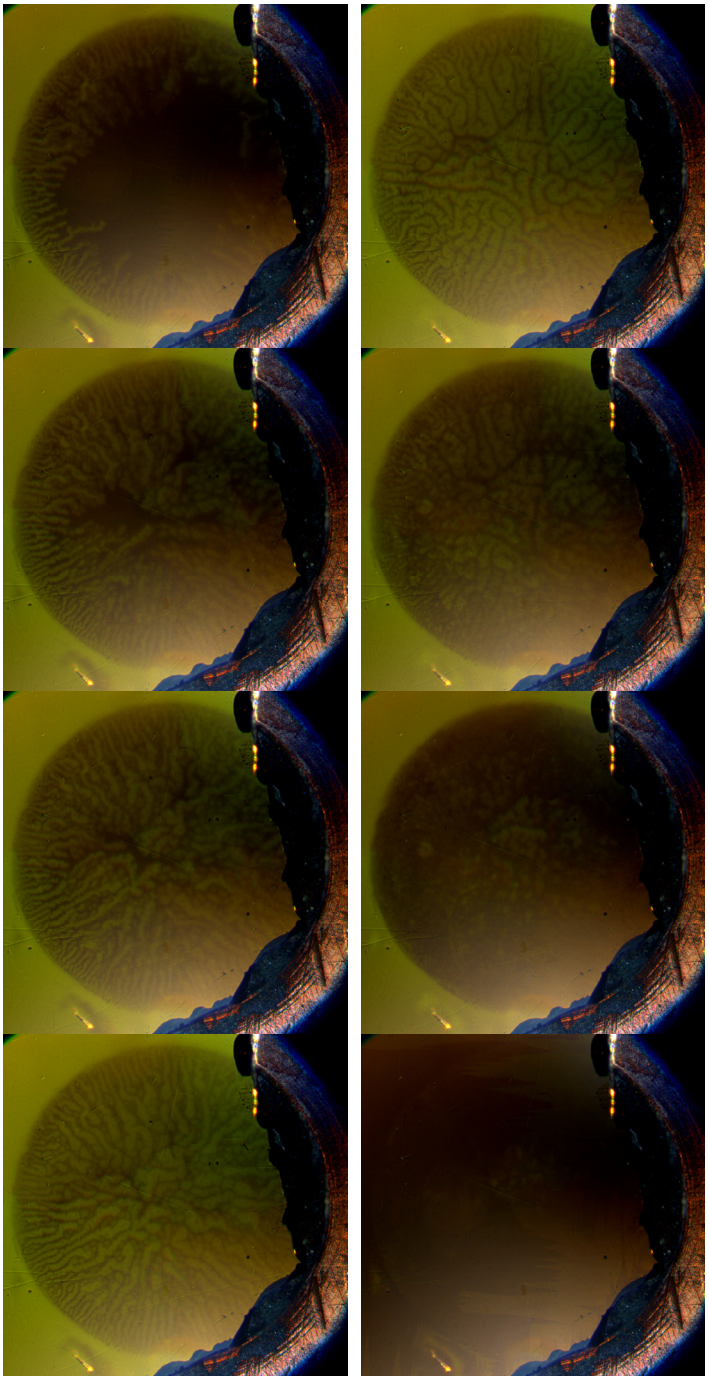

Figure 20. Field Application to a Hemisphere I. The left column shows images taken at an increasing applied field to saturation. The right column shows decreasing fields after saturation.

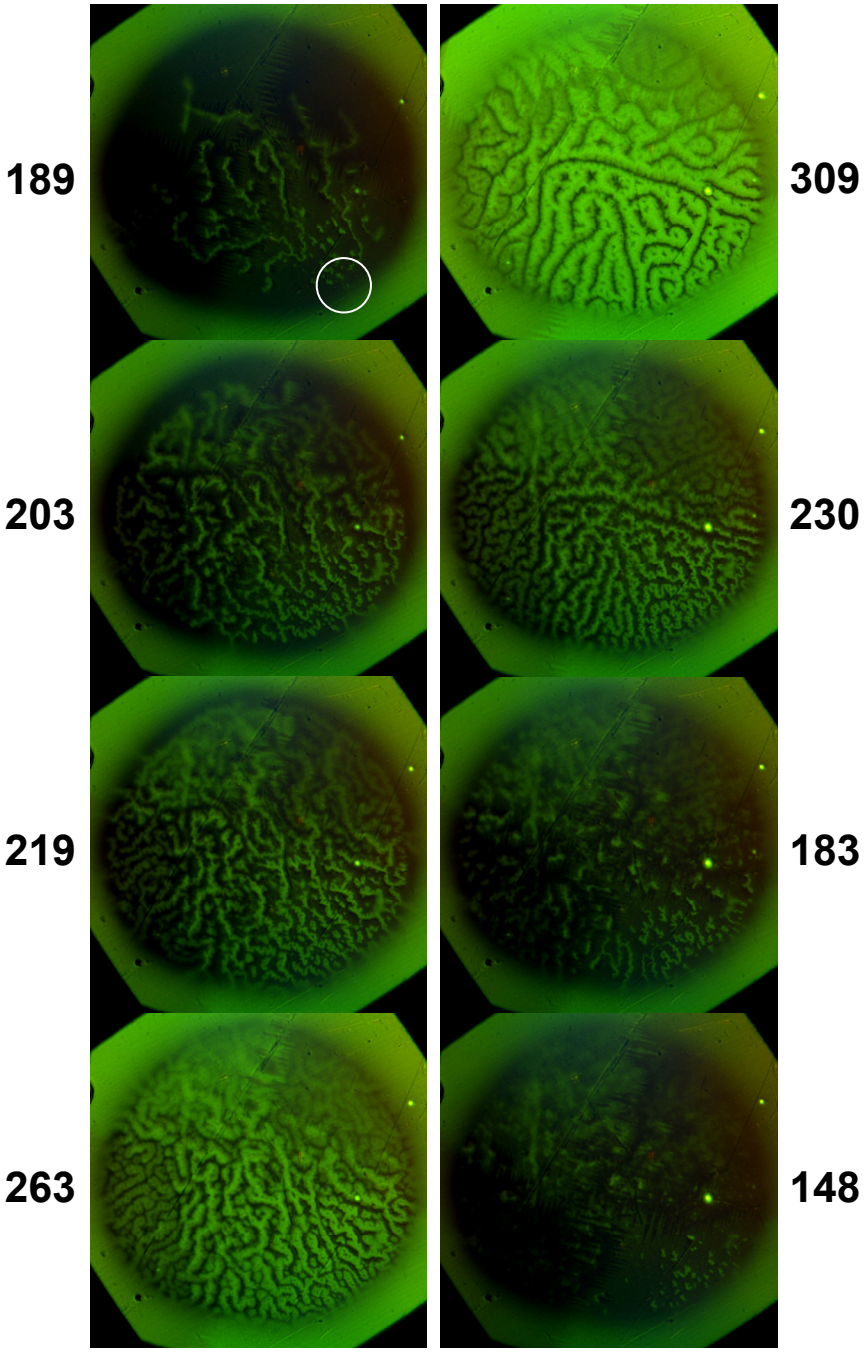

Figure 21. Field Application to a Hemisphere II. The left column shows images taken at an increasing applied field to saturation. The right column shows decreasing fields after saturation.

white. However, where the flux entered isn't very important; what is important is that at a small applied field, the flux has moved into the center of the sample. Also, in the images at 183 Oe and 148 Oe, the laminar structure has almost completely broken into the tubular structure.

The set of images shown in Figure 22 is the imaging performed on the MT crystal hemisphere. Very little tubular structure is prevalent and this structure is only in the very center of the sample at 62 Oe. Also, notice the fields at which all these images were taken. The fact that the fields are so low indicates the sample is at a temperature close to T_c (critical temperature), even though the temperature reading claimed 4.8 K. This tells us that there was a very large (roughly 2 K) temperature gradient in the sample, affecting the flux structure greatly. The sample still shows the same behavior of the flux slowly moving into the center like the other hemispheres and cones. Finally, as a side note about the flux exit of this

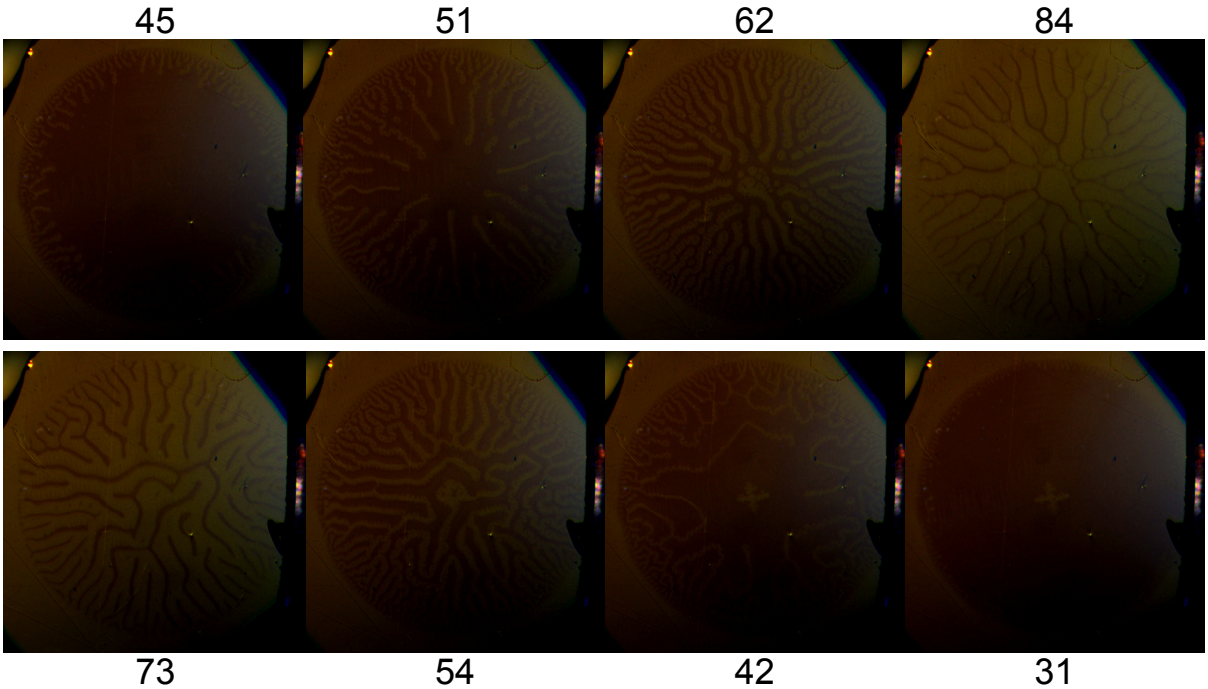

Figure 22. MT Crystal Hemisphere. The top row shows flux entry (Oe). The bottom row shows flux exit (Oe).

sample: in the center there is a small amount of flux forming an "X". On the bottom of the sample was a small divot that is directly correlated to flux pinning. This is further evidence showing the effect of a small physical defect on the remnant flux in a sample.

As there was with the cone, there are questions that remain. Why does the flux move into the sample in these ways? What is the full effect of pinning on the flux structure? What is the preferred flux structure? These questions, and others, will be addressed in the Discussion chapter for each sample shape.

3. Applied Current Experiments

The previous section contained a discussion about the effect that an applied magnetic field has on a superconducting Pb strip (Figure 16). The second half of my research has focused on ascertaining the effect that an applied electrical current has on the intermediate state flux structure present in that strip. The immediate answer here is that the magnetic flux inside the sample moves according to the Lorentz force as was discussed in the aforementioned section. The addition of a driven current on top of the supercurrents inside the sample causes a change in the magnetic flux structure. The Lorentz force equation not only demands a motion of the flux, but this motion must be perpendicular to both the applied field direction and the direction of the applied current. This fact has been known[33] and utilized[17] from very early in superconductivity research. Notable work was performed by Solomon[34] in 1967. He studied a system of two thin superconducting strips separated by an insulating material. A small external field was applied, and then current was passed through one of these strips. A voltage response was measured on the second strip indicating a consensual motion of flux tubes. (Refer to Figure 23 for Solomon's experimental setup.) We

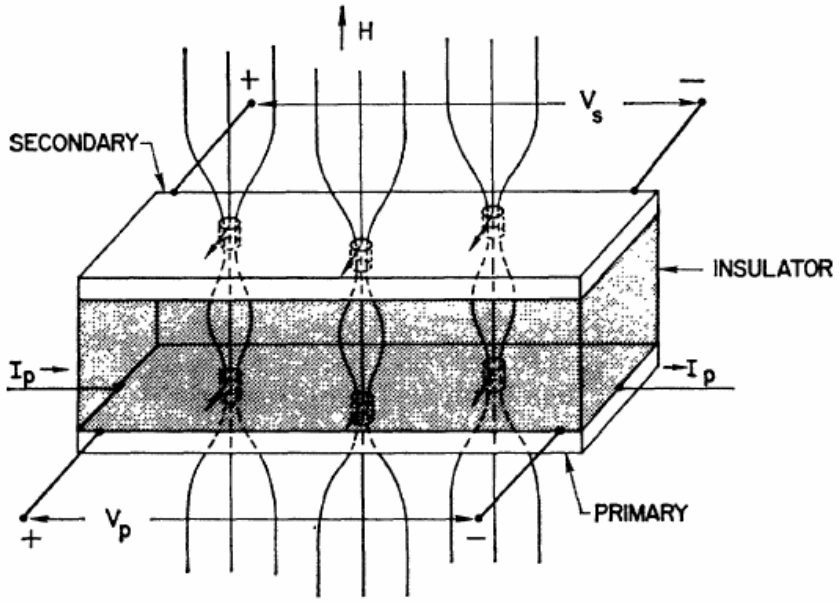

Figure 23. Solomon Experiment. The image is of the sample setup[34] with the primary and secondary superconductors separated by an insulator.

have verified this general motion. However, whether or not the flux moves is not the focus of this research. I am studying how the flux moves, and how the application of current affects the magnetic flux structure in the intermediate state.

I have made multiple attempts at imaging the magnetic field inside a superconducting Pb strip during the application of current. In this section, I present images from various samples. I also address the many obstacles I have encountered while trying to image these samples. All the following samples were cut in the fashion described in the Sample Preparation chapter, and only those cut from the Alfa Aesar films are shown.

Figure 24 shows a Pb strip that has a constant applied current of 0.3 A. The current is applied along the vertical axis of the images. Actual direction (up or down) is not important here as we do not distinguish whether the applied field is directed into or out of the images. The edges of the sample are dark (superconducting) vertical lines on either side of the magnetic flux structure. In this series of images, I am changing the applied field. The sample

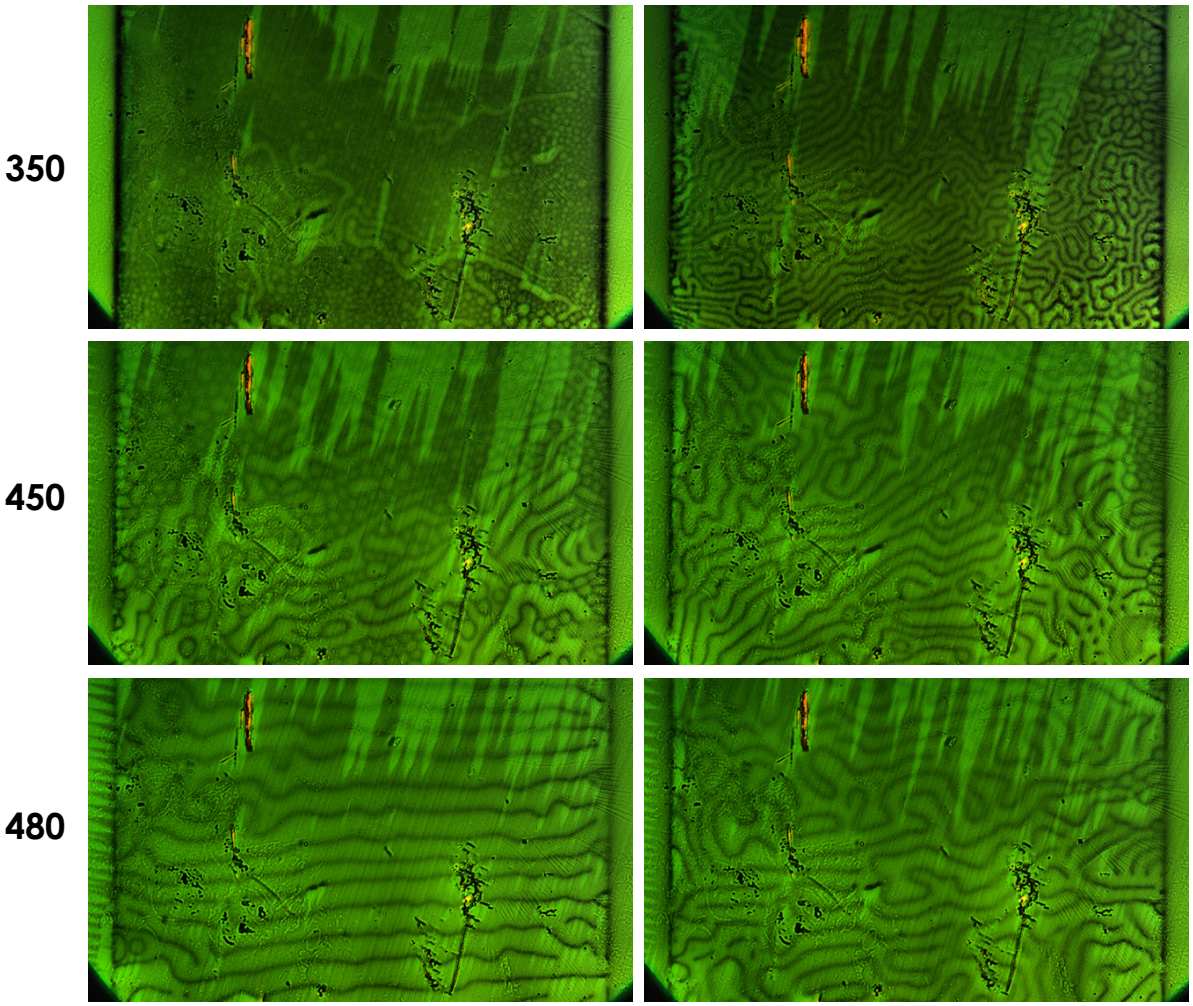

Figure 24. Strip with Constant Current 0.3 A. A constant current of 0.3 A is applied while the external field (Oe) is changed. The left column is increasing in field and the right column is decreasing.

was originally ZFC, the current applied, and the field increased (left column) to saturation. As has been done in other samples, the applied field was then decreased (right column) after saturation. The numbers to the left indicate the field (Oe).

Initial observations of the images in Figure 24 provide many effects to consider. Foremost, the sample shows a mixture of both flux tubes and flux laminar. Because we have only seen this in samples that were not clean Pb crystals, the assessment that this strip contains pinning can be made. The next important detail is contained in the increasing field

480 Oe image. Here we see what could be the pseudo-laminar structure that I mentioned in regards to Figure 9 of the previous section. The flux density is high enough that the tubular phase is not energy efficient. What is very different from either Figure 9 or Figure 14 (both show actual laminar structure) is that the structure in Figure 24 is perpendicular to applied current. This structure will be referred to from here on as the "stripe pattern." It is important to remember that this image is a still-shot of magnetic flux in motion (motion is right to left in this case). While the perpendicular flux flow is not surprising, the structure created by the motion of the current is. It is puzzling that the superconducting avenues, which offer no resistance to the current, are in this case also perpendicular to the direction of current flow. There are superconducting avenues for current flow along the edges, but whether these regions provide enough Lorentz force to create this pattern is yet to be seen.

The 480 Oe image on the decreasing (right column) side does not quite resemble its increasing counterpart. It is, however, much like the laminar structure that would be expected after saturation. More interestingly, though, are the other two decreasing field images. At both 450 Oe and 350 Oe there appears some flux tube structure at the right edge of the sample. At a specific range of applied field and applied current, there is a nucleation of magnetic flux tubes at the sample edge. This is arguably the most interesting effect that current has on the flux structure.

To further examine these effects, Figure 25 shows the same sample as Figure 24, but at a higher applied current, 0.5 A. As in the previous set of images, these show a constant applied current with an increasing (left column) and decreasing (right column) applied magnetic field. In general, there is a similar reaction to the current. At higher fields (290 Oe

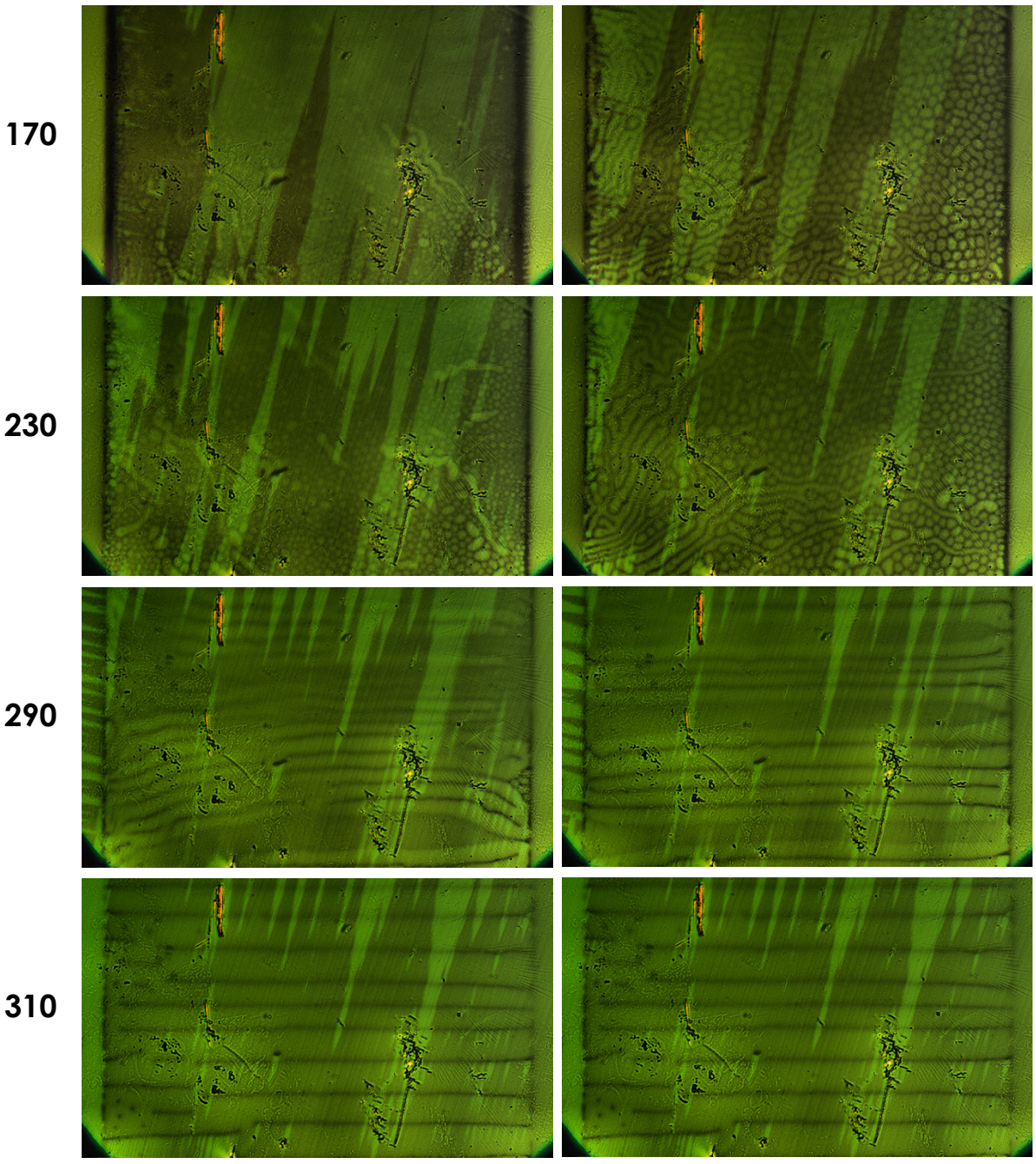

Figure 25. Strip with Constant Current 0.5 A. A constant current of 0.5 A is applied while the external field (Oe) is changed. The left column is increasing and the right column is decreasing.

and 310 Oe) the flux motion induces the stripe pattern phase. Also, at 310 Oe, the stripe pattern is clearly defined with superconducting lines parallel to each other. The blurry areas in the 290 Oe images are actually superconducting, corrugated lines that are oscillating too quickly to be caught on camera, which takes images at 30 frames per second. The speed of oscillation is indeterminable with the available equipment. Of important note in the 310 Oe images is the breaking of the superconducting lines along the left edge of the sample. A similar effect was observed by Solomon and Harris[33].

Similar to the Figure 24, the motion of flux is right to left. Also, in the decreasing column at 230 Oe and 170 Oe, instead of full laminar structure the sample contains a majority of flux tubes. This is because with a higher current, nucleated flux tubes are forced across the majority of the sample and create a dynamic tubular structure. Again, this motion is difficult to fully observe in still images. Before an attempt to properly show this motion is made, however, one other aspect of Figure 25 needs to be understood. The stripe pattern shown appears at 290 Oe, and the sample is nearly saturated at 310 Oe. This saturation occurs at a field nearly 200 Oe lower than the saturation in Figure 24. The reason for the discrepancy is that an applied current heats the sample. While each set of images was taken at a constant temperature, there is a difference in temperature between the two data sets. The higher applied current in Figure 25 brought the sample to a higher temperature than was measured for Figure 24 and therefore, Figure 25 shows the sample at a point in the H-T phase diagram (Figure 4) that is closer to the normal region, so the applied field required for saturation is smaller.

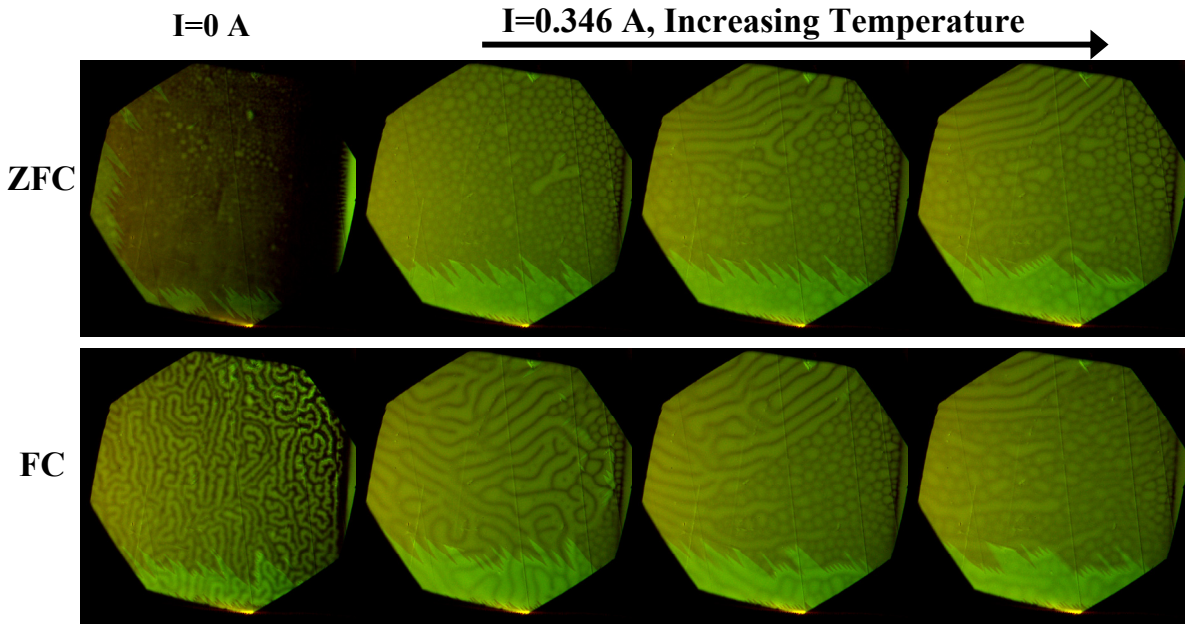

Figure 26. Motion Over Time. Showing motion of nucleated flux tubes at constant field and current with increasing temperature. The top row was ZFC, the bottom was FC. The left most images were taken at 0 A applied current. The rest of the images were taken at 0.346 A over increasing time (left to right).

While it is important to always consider the effect that an applied current has on the temperature of a sample. I have discussed it in detail here in order to provide a series of images depicting flux tube nucleation. Figure 26 shows a Pb strip which, after being brought to a constant applied field, was brought to a constant current, and allowed to increase in temperature bringing the sample closer to the normal state. Each row of images shows this increase in temperature over time (left to right). The top row of images was taken after ZFC the sample, while the bottom row images were taken after FC. In each of the images, the right edge of the sample is visible and flux flow is again right to left. The two images at the left show the sample at a constant applied field without an applied current in order to depict the original state of the flux structure. Each subsequent image (left to right) show the sample held at a constant 0.346 A with the temperature increasing. The motion of flux is most evident in the bottom row as nucleated flux tubes move across the sample replacing the

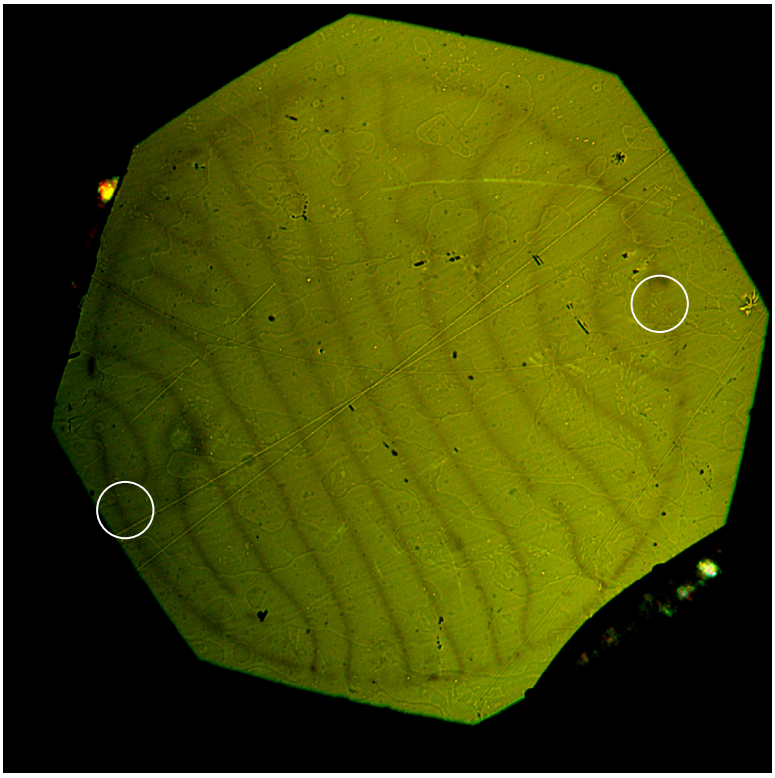

Figure 27. Pb Disc with Current. Applied current in MT 100 Pb Crystal Disc. The white circles denote the current contacts.

laminar structure that was already in place. In addition, each of the four images to the right show a curved stripe pattern toward the top. This stripe pattern is an effect caused by a temperature grading resulting from a point connection from the current lead. The lead connection is hot from the resistance in the copper wire and heated the sample in a non-uniform manner. The direction of flux flow can be attributed to being perpendicular to the flow of current from the current lead's point source.

The response of magnetic flux flow direction to the direction of an applied current was best observed in my attempt to apply current to a Pb crystal disc. Shown in Figure 27 is the MT 100 Pb crystal disc at an external magnetic field of 300 Oe and current of 0.123 A being applied. The white circles are the points at which current leads are connected. The leads have been connected along the side of the crystal as to not interfere with the placement

of the indicator. In all areas, the stripe pattern is perpendicular to the flow of current. Because of this, the highest distortion is found around the edge of the sample, and around the current leads.

The data found in Figure 24 through Figure 27 has lead to many interesting questions. While the question of why the flux flows has been answered, the question of how isn't yet absolutely clear. Also, their needs to be a proper determination of the effect that temperature has on this system, and because current plays a large role in temperature, this is not trivial. The actual flow of the applied current, specifically the flow of current through the stripe pattern phase, is not clear either. Finally, an exploration of the mechanism by which the driven current causes tube nucleation is needed. All of these issues will be discussed in the Discussion chapter.

CHAPTER IV. DISCUSSION

Up to this point, only the visual observations that are the product of the research conducted have been presented. In this chapter, I discuss the analysis that I have performed on these observations along with the ascertainable physical implications. More directly, I discuss the effects of the intermediate state flux structure on the magnetic hysteresis, the relationship between the dense tubular structure and the physics of foams, and the effects of an applied current in more detail. I will begin, however, with a general analysis of the observables discussed so far.

1. Imaged Observables

This discussion will begin with the Pb crystal discs which were shown to be the samples exhibiting the clearest reaction in the imaging. The first manifestation of the intermediate state in an applied field is the finger-like flux penetration that occurs at all of the edges around the sample. We have seen and briefly discussed this in the last chapter (Figure 10 and Figure 12). The flux first enters the sample by penetrating the corners of the sample. This creates the finger structure and continues until the structure reaches a maximum length and nucleates a tube. The resulting flux tube is driven into the center of the sample. A measure of the length of this flux entrance supports this explanation of tube nucleation. This measure is shown in Figure 28. Note that there are three separate sections to this plot. The first section, at the left of the plot, is the increase in length of the flux penetration. This growing of the flux entrance is associated with the increase in applied field and occurs before any flux tubes are created. Following this increase is a plateau in the plot. This plateau represents the brief period where the flux entrance has reached its maximum value. The

decrease in flux entrance length that follows is roughly linear and is the result of a combination of an increasing central flux structure with a diamagnetic Meissner band that is

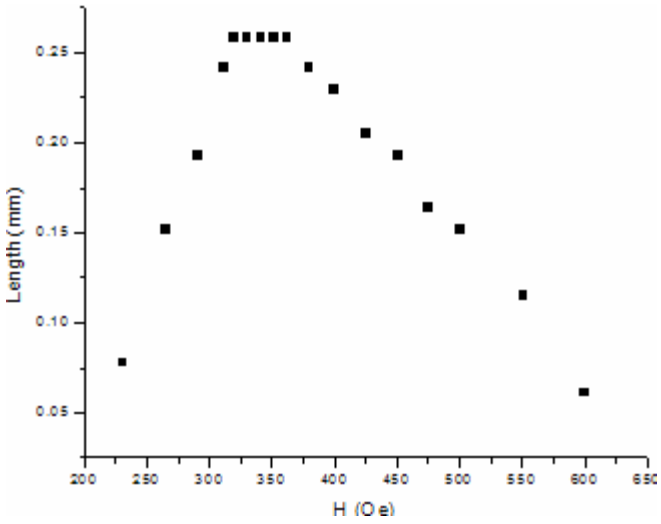

Figure 28. Flux Entrance Length. Initial flux penetration grows to a terminal length. It then decreases linearly to zero.

only slowly decreasing in width.

The central structure (Figure 9) comprises of flux tubes that are being forced into the center by the Lorentz force, but also have a repulsion force with neighboring tubes. This combination of forces creates a disc of stacked flux tubes with an overall growing diameter. This growing disc of normal flux tubes creates a diamagnetic band that carries the supercurrents. As the disc grows, the band decreases. Figure 29 shows the growth of the normal disc diameter and Figure 30 shows the creation of and decreasing width of the diamagnetic band. In both plots, *h* is the unit-less reduced field, $h = H_a / H_c$. Remember that both crystal discs have a 5 mm diameter. Also, the zero points were not included in the measure of central structure diameter as it didn't exist below *h=0.45*, while the diamagnetic superconducting structure existed and only decreases in the beginning because of the increasing flux penetration. The creation of flux tubes is, however, evident in Figure 30 as

the significant drop in width that occurs at *h=0.45*. Also, notice that while both structures change dramatically between *h=0.45* and *h=0.65*, increasing the field above *0.65* results in

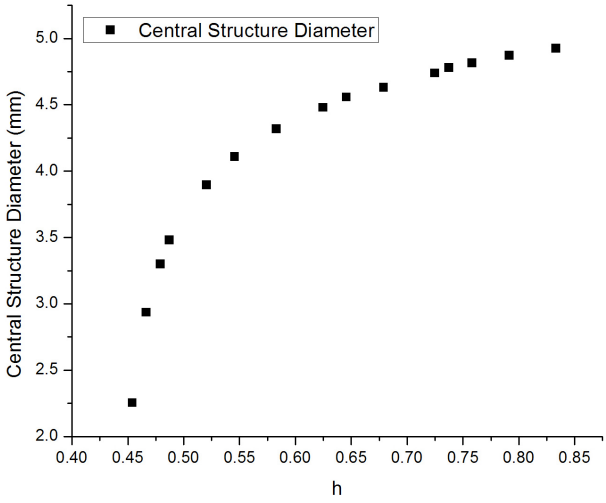

Figure 29. Central Structure Diameter.

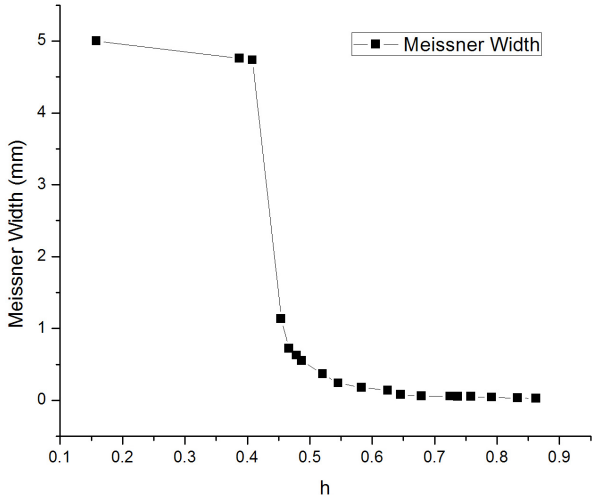

Figure 30. Meissner Width.

roughly linear changes. This explains the linear decrease in flux penetration length in Figure 28.

We can also plot the average diameter of the flux tubes themselves as a function of the applied field. Figure 31 shows an overall increase in tube diameter. This measurement required taking an average of the tube diameters. Throughout every image, however, there existed many tubes with a very large range of diameters. At the highest *h*-value, the range of diameters was greater than 0.1 mm and the mean diameter was 0.13 mm. With such a large range, the mean diameter was determined by the percentage of tubes at each end of the range. The blue line shown in Figure 31 is the theoretical tube diameter increase proposed by Goren and Tinkham[35] in 1971. It is not a fit of the measured data. Goren and Tinkham postulated that the diameter would grow as $D = [2\delta d/(1-h)(1-h^{1/2})]^{1/2}$. In this equation, d is the sample thickness (1 mm) and $\delta = (\xi - \lambda)$, which is known as the wall parameter. For δ, the

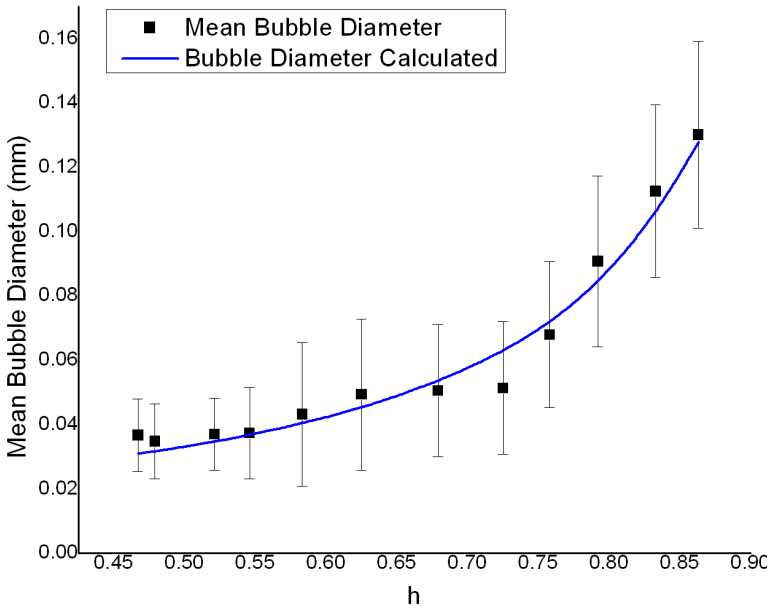

Figure 31. Flux Tube Diameter. The black squares are measured data, and the blue line is the theoretical fit of, $D = [2d \cdot \delta /(1-h)(1-h^{1/2})]^{1/2}$.

experimental value[13] of 80 nm was used. The plot shows a very good fit, and until now, this trend had only been hypothesized and not observed experimentally. There are papers[23,24,27,28] that state the tube diameter does not grow in response to an increasing applied field. This lack of growth simply shows that the measured samples are too highly pinned and the tubes are not allowed to grow without deformation[28].

The last plot relevant to the Pb disc is the measure of the laminar width in decreasing fields. This measurement has been performed before[23] and has a sound theoretical base in Landau's description of laminar domain structures. The width of the normal domain, a_n, can be described through flux conservation[13]: $a_n = a * H / H_c$, where a is the overall periodicity length and the sum of the normal domain width and the superconducting domain width. The periodicity length, a, can then be described by $a = [\delta \cdot d / f(h)]^{1/2}$, where $f(h) = (1/4\pi)[(1+h)^4 \ln(1+h) + (1-h)^4 \ln(1-h) - (1+h^2)^2 \ln(1+h^2) - 4h^2 \ln(8h)]$ and is

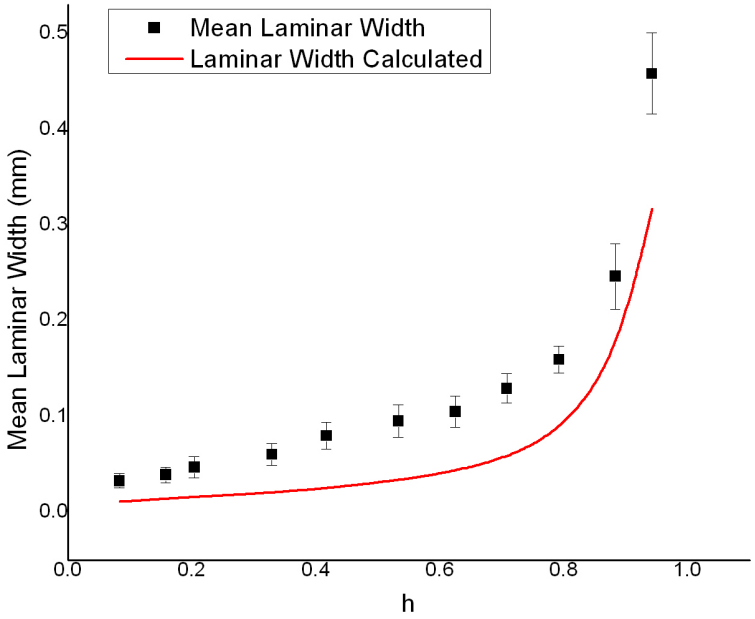

Figure 32. Laminar Width. The black squares represent the measured data. The red line is the calculated laminar width, a_n.

known as the Landau function (see Fortini and Paumier[36]). Figure 32 shows the measured data (black) and the calculated data (red) of the laminar structure width in the Pb crystal. The data points were taken in decreasing field from the normal state (Figure 14). As superconducting lines first enter the sample, there is a sharp decrease in the laminar width. Also, the extrapolated line (when approaching $h=0$) does not go to zero length. This is because the last of the laminar structure to leave the sample still have a finite width.

The last question I would like to address is about the motion of the flux — not of the slab as that motion has been evident — but the motion inside the cone and hemisphere. Let us start by making the assumption that flux tubes are the topology created in these samples as well (this assumption is valid as there are flux tubes found in both types of samples). This flux tube has an associated wall energy per unit area[13], α, discussed in the Introduction chapter, $\alpha = (H_c^2/8\pi)(\xi - \lambda)$. We should be able to calculate the energy required to create

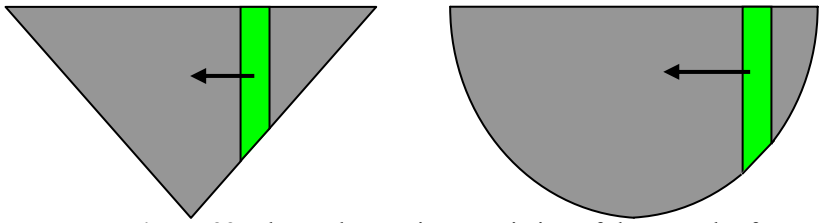

Figure 33. Flux Tube Motion. Depiction of the growth of a flux tube as it travels into a hemisphere or cone sample.

the flux tube by multiplying this α by $2\pi rl$, where r is the radius of the tube and l is the length of the tube and (for a constant r) the determining factor for the total wall energy. For a slab sample, l never changes and thus after a flux tube is created, no extra energy is required in moving it. For both the cone and the hemisphere, however, as a flux tube moves into the sample, l increases and the flux tube requires more energy (Figure 33).

Looking first at the cone sample, l increases linearly with motion. We can describe this motion by $l = x \cdot \frac{D}{R}$, where x is the distance traveled, D is the final depth of the sample and R is the sample radius. Remember that flux tubes moved slowly into the center of the cone (and the hemisphere) with the increasing applied field (Figure 18, Figure 20 and

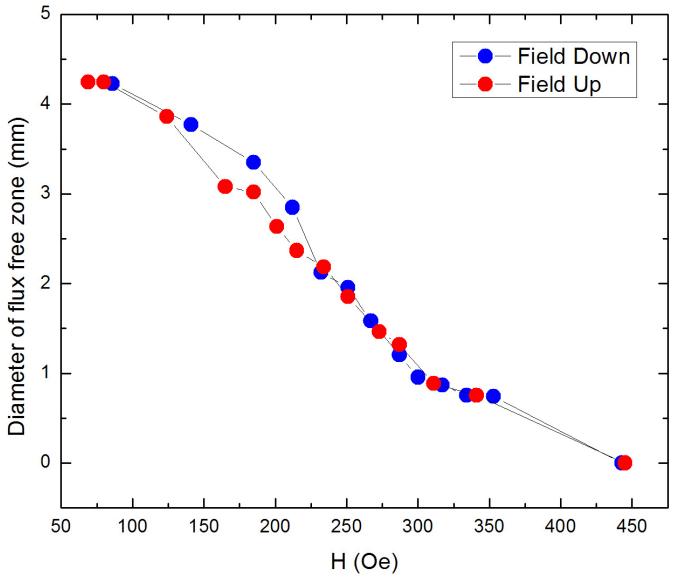

Figure 34. Diameter of the Flux Free Zone in a Cone.

Figure 21). Figure 34 shows the diameter of the central flux free Meissner state as the applied field is both increased and decreased. The shape of the plot is not surprising. The plot is linear because the diameter of the flux free zone relates directly to the distance the flux has moved inward from the sample edge. This also shows that the energy required to increase the length of the flux tubes comes directly from the applied field. Notice also that the flux movement follows the same line in decreasing field as well. Not only does this help support the fact that the required energy is coming from the applied field, but this shows sample reversibility.

Similar plots can be produced for the hemisphere samples. The length of the flux tube is not a linear function of the distance traveled, though. For a hemisphere, $l = \sqrt{2Rx - x^2}$, where, again, R is the radius of the sample and x is the distance traveled by the flux tube. If we solve this for $x(l)$, and then recognize that for an assumed radius (2.5 mm), we can solve for $D_{ff} = 5 - 2 \cdot x(l)$, where D_{ff} is the flux free diameter as a function of the tube length. Figure 35 shows two separate plots. The left plot shows $D_{ff}(l)$. The right image shows the

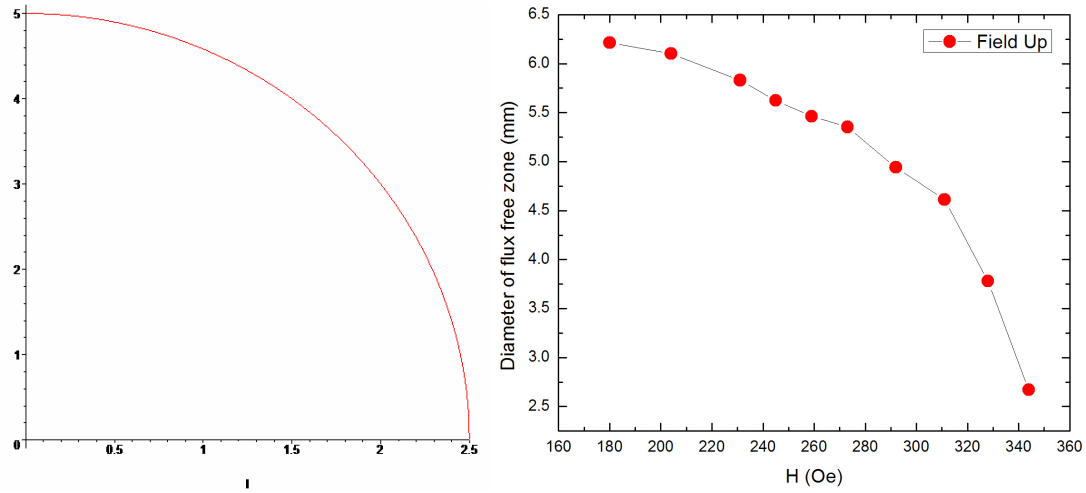

Figure 35. Diameter of the Flux Free Zone in a Hemisphere. The left plot is D_{ff} vs l. The right plot is the measured diameter of the flux free zone.

measured diameter of the flux free zone for a hemisphere as a function of applied field. Just as in the cone sample, there appears to be a linear relationship between the length of the tube and the applied field.

2. Topological Hysteresis

After taking a close look at the intermediate state flux structures, it's important to look at the overall magnetization. It was stated earlier that the magnetization of different shape Pb samples was recorded by Provost *et al*.[29]. However, Provost focused purely on the penetration field. Because slab shapes (shapes with a geometric barrier) create flux structures that are vastly different for flux entrance and exit, one should ask whether this difference between open and closed topology affects the overall sample magnetization.

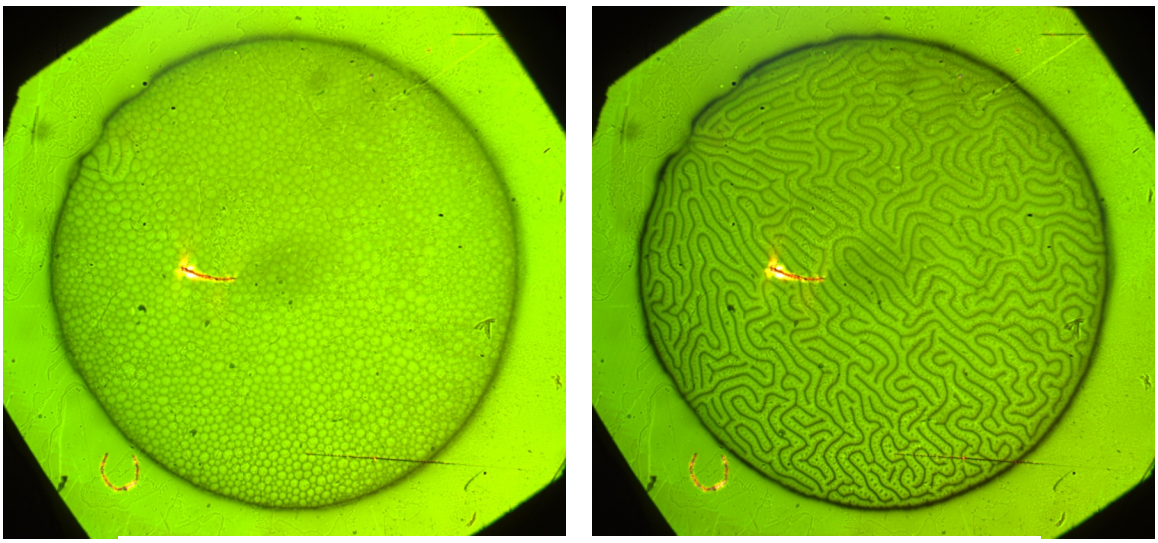

Figure 36. Open and Closed Topologies. The left image shows the tubular phase structure, while the right images shows the Landau laminar structure.

Figure 36 serves as a visual reminder of the differences between the two flux structures of the intermediate state. The Pb disc in both images is at the same thermodynamic equilibrium in the H-T phase diagram. The left image shows the tubular structure, while the

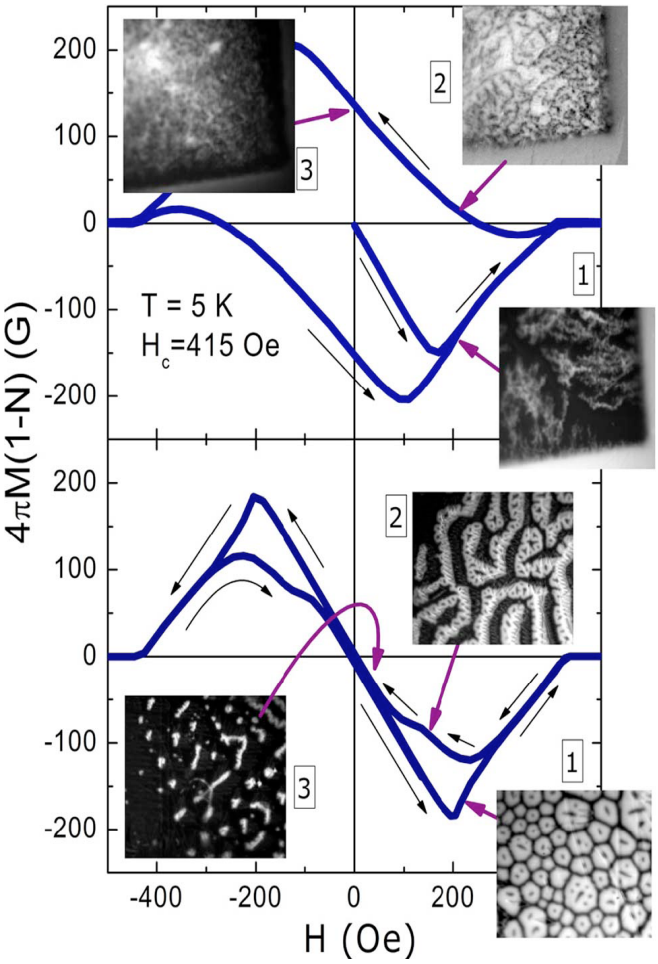

Figure 37. Magnetization Loops. Shown are stressed (top) and stress-free (bottom) samples. MO images were taken in the order corresponding to the numbering.

right image shows the laminar structure. The only difference in the preparation of each image is the path taken to reach intermediate state.

When discussing the overall magnetization of Type-I superconductors, magnetic hysteresis is common in measured magnetization loops. This hysteresis is commonly attributed to defects or impurities in the superconductor. However, even the cleanest samples seem to exhibit some amount of hysteresis. Through a combination of measured magnetization loops and the MO experiments, it has become clear that the magnetic hysteresis is likely an effect to be attributed to the flux structures in the intermediate state.

Figure 37 demonstrates the magnetic hysteresis observed in Type-I superconductors. Two samples of similar dimensions were measured. In each set of images, the number corresponds to the order in which they were taken, and the arrow indicates the analogous point along the magnetization loop. The top loop represents a sample that had been cold-rolled and was extremely pinned. This pinning can be seen not only in the amount of magnetization left over at zero applied field, but also in the structure that the flux takes. The

flux enters the sample non-uniformly and in a very dendritic fashion. The bottom loop, however, shows a clean (pinning-free) sample as is indicated by having nearly zero magnetization at zero applied field. Clean as the sample is, however, there is still an associated hysteresis at intermediate fields.

Figure 38 images a more detailed description of the clean-sample hysteresis. Again, the numbers indicate the order of the images, while the arrows depict their corresponding points along the magnetization loop. If we follow the loop, we see that initial magnetization (blue line) behaves exactly as a Type-I superconductor. There is an increase in the magnetization magnitude until flux enters the sample (approximately 120 Oe). As more flux enters the sample, the magnitude of the magnetization decreases and approaches zero as the flux density nears the normal state. While decreasing the applied field (green line), however, there appears a hysteresis. First, though, the magnetization line follows the original increase. Notice that this occurs during a period of time where the amount of flux inside the sample is

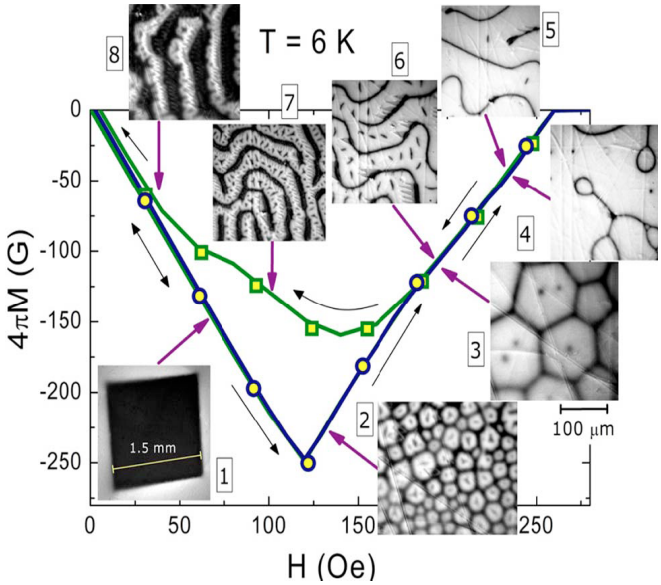

Figure 38. Topological Hysteresis. Magnetization loop of a stress-free sample. MO images were taken in the numerical order shown. Circles are the ZFC data and squares are the FC data.

very dense. Comparing images 38(4) with 38(5) and 38(3) with 38(6), one can see the hysteresis begins when the density of normal flux begins to differ between flux exit and entry. As we've seen before (Figure 14), the laminar structure does not leave the sample completely until the applied field nears zero. It appears that it is this propensity for the laminar structure to stay in the sample below $H_a = (1-N)H_c$ that is causing the hysteresis.

If a comparison of the magnetization loop in Figure 38 is made with the magnetization loop in Figure 5, there appears to be a dependence on sample shape as well. This is another argument for the propensity of the flux tube structure. The lack of hysteresis in the Pb sphere indicates that the flux structure is tubular, and if this assumption can be made, it is possible to say that the laminar structure is a consequence of the geometric barrier.

A quantitative evaluation of the magnetization from the MO imaging can be achieved by calculating the total magnetic moment using $4\pi M = \int [H - B(r)] d^3 r$, where M is the magnetization, H is the applied field and B is the internal field. Because the magnetic induction is linearly proportional to the intensity, M can be calculated by integrating the MO images while calibrating using the initial slope of the measured M(H) loop. The M(H) loop that resulted from this technique is shown (blue) in Figure 39. The original measured magnetization loop (red) is shown in comparison. The two loops are in good agreement.

Figure 40 shows the profiles of magnetic induction that has been measured for both the laminar and the tubular pattern formations. It has been generally accepted[14] that the field inside the normal domains of the intermediate state is close to H_c. These profiles suggest otherwise and might help to serve as an explanation for the observed topological hysteresis. The field inside the laminae is close to H_c, but the field inside the tubular structure is not. It is

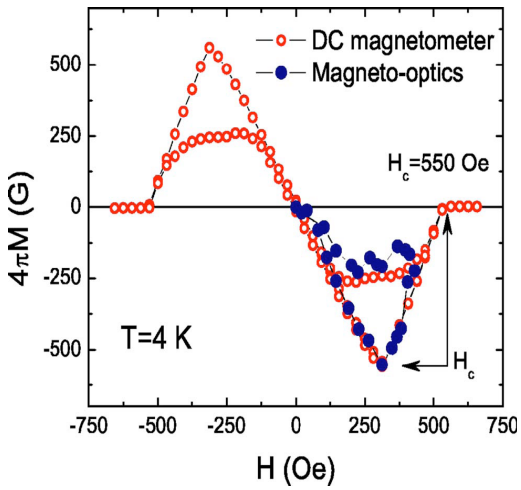

Figure 39. DC Magnetization Comparison. Loops were measured by the magnetometer (red) and reconstructed from the MO images (blue).

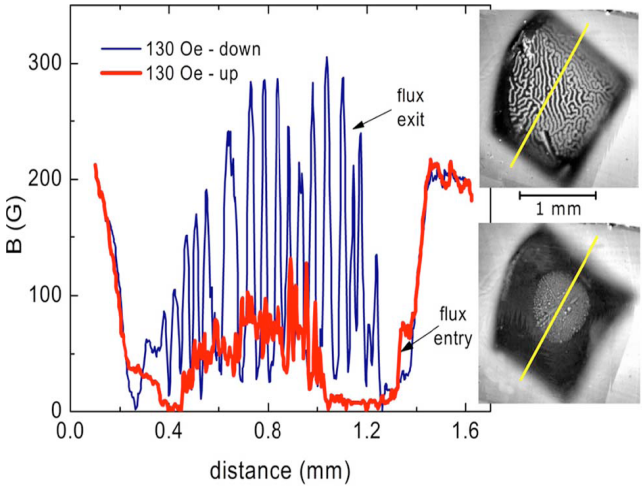

Figure 40. Magnetic Induction Profiles. Profiles were measured at T = 4 K. Corresponding MO images are shown at the right.

true that the measurements were made at a distance of approximately 10 μm from the surface. The resulting reduction in the measured fields does not account for the reduced fields that are observed. A possible explanation for this reduction could be the widening of flux tubes at the sample surface[13], but why wouldn't that take place in the laminar structure?

Another explanation might be that the magnitude of the magnetic flux inside each tube is conserved and in order to minimize the magnetic field energy, the radius of the whole tube becomes larger as it approaches the sample center. However, rigorous evaluation of the free energy of even a single flux tube is difficult as there is no sharp interface between the superconductor and the tube interior. This decreases the total free energy (Figure 1). At large distances, tubes repel each other, and start to attract when their "cores" overlap. Also, the average magnetic field increases as the tubes merge together, and the observed topological hysteresis persists only as long as the field inside the tubes is less than H_c. The approach to H_c of the magnetic field in each tube results in a honeycomb lattice orientation of the flux tubes. This lattice and its relation ship to the physics of foams is the focus of the next section.

The MO imaging can also be used to image the shielding currents and their densities via a fast-inversion method as described in Prozorov[21].

Finally, it should be noted that topological hysteresis, while not explicitly examined, was observed by Solomon[34] in the experiment mentioned in the Experiments chapter. As I stated before, Solomon measured the voltage response of a secondary superconducting strip that was separated from the primary superconducting strip by an insulator (Figure 23). A current was applied to the primary material while both primary and secondary strips were exposed to an external magnetic field. Solomon found that there resulted a hysteresis in the voltage measurements between the increase and decrease of applied current. The most prominent hysteresis observed is shown in Figure 41 and was measured at 540 G (gauss). Because this was done at such a high field, it is likely that the sample was saturated and the hysteresis observed is topological. As Solomon states:

> "Hysteresis was sometimes observed in the primary and secondary voltages…. If current was passed through the primary a second time, the curves for increasing and decreasing current were identical with the initial curve for decreasing current…. The hysteresis could be re-established by turning the magnetic field off and then on again…. The hysteresis seems to be caused by the rearrangement of the topology."

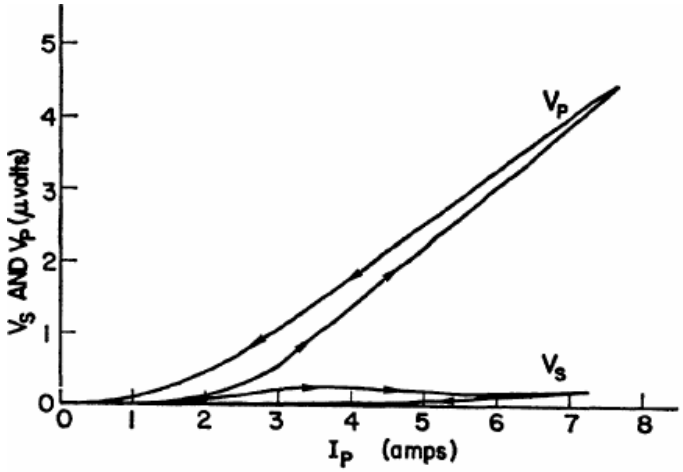

Figure 41. Solomon Voltage Hysteresis. A hysteresis is observed in the primary (V_p) and secondary (V_s) strips in voltage measurements for increasing and decreasing currents.

3. Suprafroth

Because the two-dimensional view of the tubular phase in the intermediate state resembles soap bubbles growing and merging as the applied magnetic field is changed, it is sometimes referred to as the "bubble phase". As it turns out, this phrasing is an accurate portrayal of the physics of the tubular phase. In a two-dimensional view, the tubular phase behaves like soap froth and follows very similar physical equations.

While the physics of froth has been researched for many years[8,40], in a majority of cases the coarsening and evolution of these froth structures resulted from liquid drainage between cells and the diffusion of vapor molecules with time as the varying parameter. In this system of suprafroth (named[37] so in allusion to superconductors being called "supraconductors" in the 1920's and 1930's), the mechanism for structural change is a dissipation of coupled, Cooper pair electrons. While the coarsening variable for soap froth is time, there are two variables for coarsening in suprafroth: applied magnetic field and temperature. With coarsening variables which can be controlled (this is not the case for time), a more detailed description of the process is possible. So far, however, a limited analysis of the relation between suprafroth and time-coarsened froth has been performed.

The suprafroth structure occurs only in a specific region on the H-T phase diagram for a Type-I superconductor. The available region is described in Figure 42. This is the region in which the magnetic field density is high enough such that there is almost no diamagnetic band, but the density is not so high that the polygonal structures give way to elongated objects. This region, so far, can only be visually defined. The large insert in Figure 42 shows an example of the polygonal suprafroth structure.

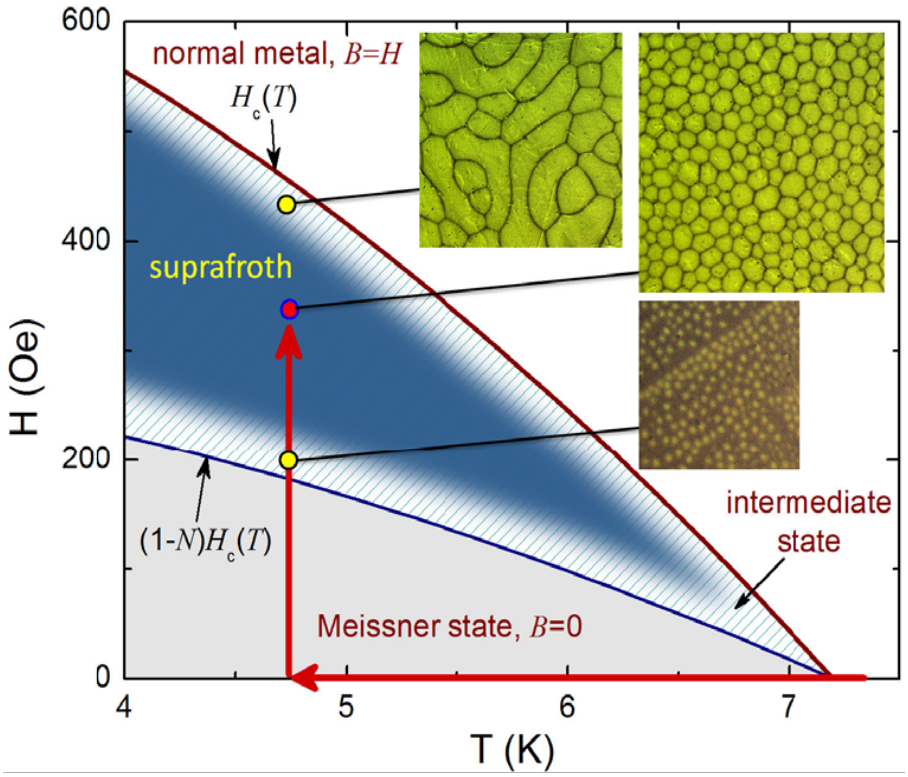

Figure 42. Suprafroth Region. The dashed region is the intermediate state with the solid region being the suprafroth phase. The large insert shows suprafroth. The two smaller inserts show the intermediate state outside of the suprafroth phase. The red arrows depict the thermodynamic path taken to achieve these phases.

This suprafroth region is created by single flux tubes penetrating the sample and being pushed towards the center. As shown before, the tubes begin to stack and coalesce. The structure is formed by a combination of positive wall energy with a repulsion force between tubes. Figure 43 shows the detailed process involved in analyzing the suprafroth structure. A region of approximately 2 mm x 2 mm of the images from the magneto-optic experiments (first row) were taken and focused upon (second row). The contrast for these close-ups was adjusted and then the images were transformed into black and white (third row). Using carbon paper, the structure — containing up to 160 cells — was traced, scanned and analyzed in terms of cell statistics (third and fourth rows).

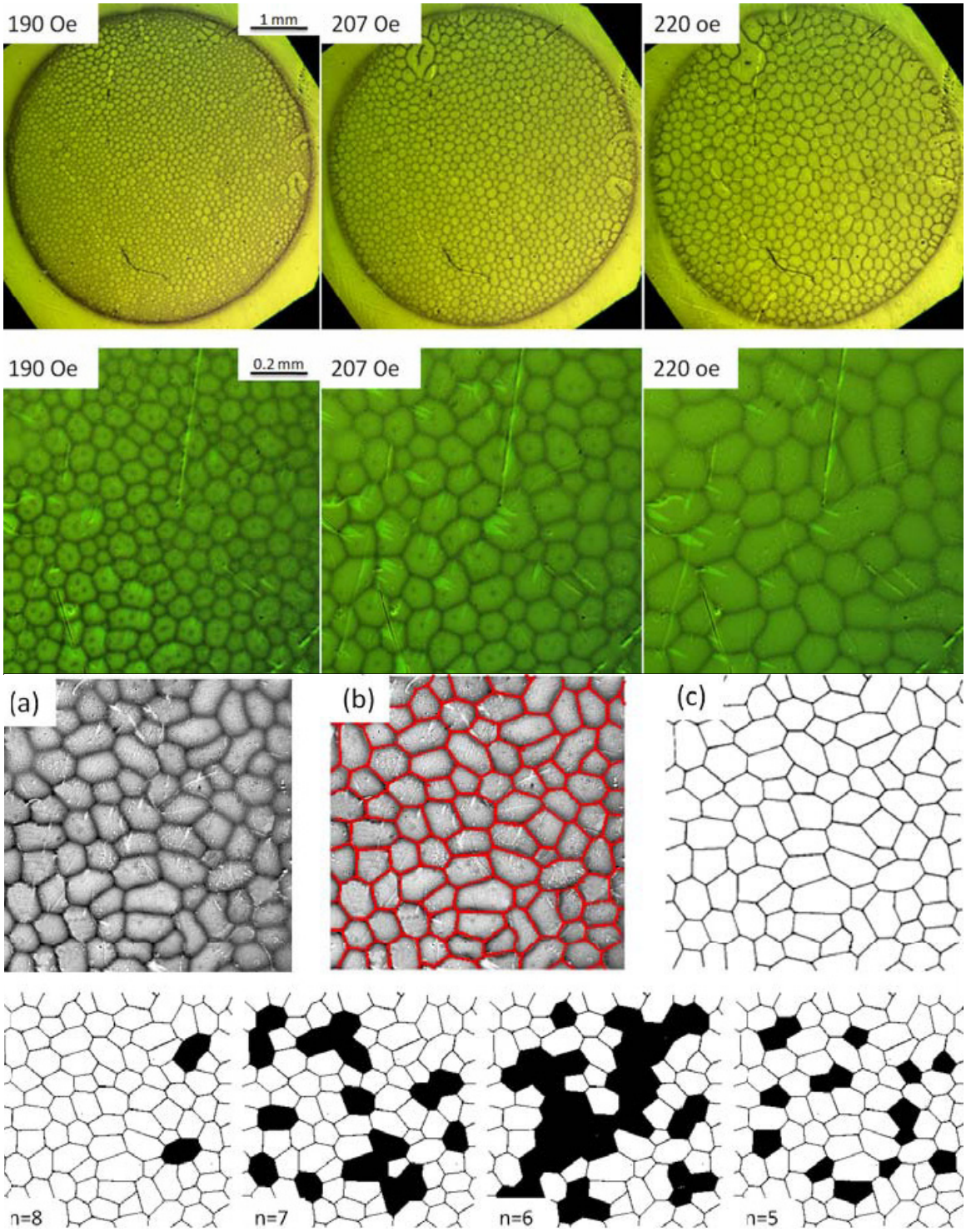

Figure 43. Cell Analysis Procedure. Each row of images represents a stage in the analysis procedure as described above.

The first aspect of the suprafroth that was analyzed was reversibility. In a majority of froth experiments, the coarsening variable is time and the experiment is irreversible. In the case of suprafroth the coarsening variables are applied magnetic field and temperature which can both be increased and decreased to check the elasticity (and hence, reversibility) of the topology. Figure 44 examines a small magnetic field loop applied to the sample after ZFC. The applied field was brought to 466 Oe and an image was taken, which is represented by the black trace. The field was then increased a small amount (ΔH is given for each image) and then returned for 466 Oe. The resulting image was traced and is shown in red on top of the original black trace.

The region enclosed by a grey square in each image is the region that is most uniform in its distribution of polygons. An experimentally new conclusion can be drawn about this region. It is the most robust area in comparison to regions with higher cell diversity. This conclusion can be directly related to the Aboav-Weaire law[38] as applied to the dynamics of cells whose neighbors have a certain number of sides. Also, the red trace is highly robust and reversible over subsequent $H \rightarrow \Delta H \rightarrow H$ cycles. Also, a similar pattern arises from cycles

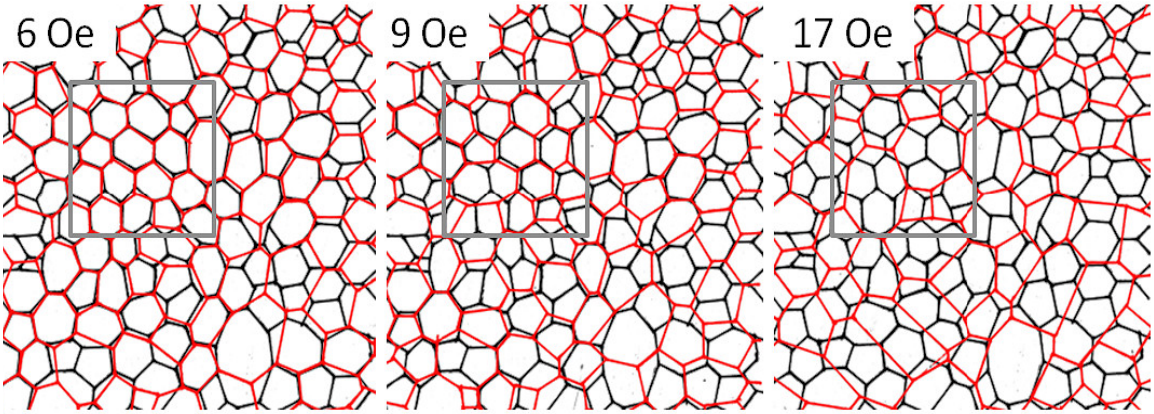

Figure 44. Structural Evolution of Suprafroth. Each image depicts a loop in the applied field with ΔH shown. The grey square represents the most reversible region.

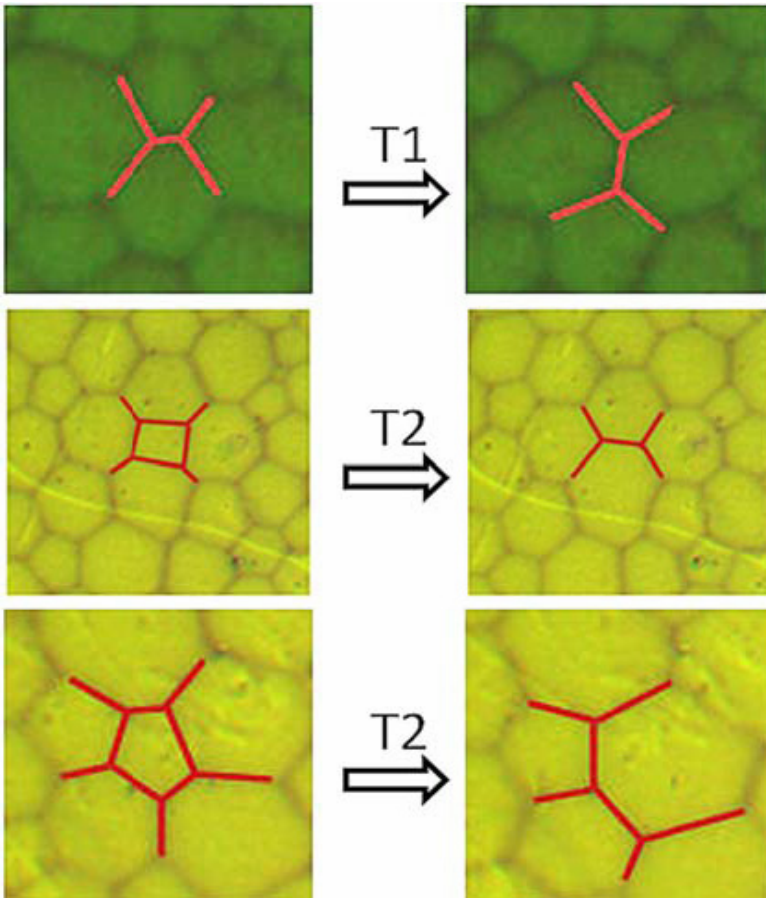

Figure 45. Cell Transformation. The images show examples of both T1 and T2 transformation.

over which the change in magnetic field is negative.

It is also important to identify the suprafroth tube transformation/coalescence process in relation to conventional froths. In traditional froths, there are two types of bubble transformation: T1 (cell sliding) and T2 (cell collapse). Figure 45 shows examples of both processes occurring inside the suprafroth exactly as they occur in coarsening soap foam.

A quantitative measurement of the distribution *n*-sided polygons is shown in Figure 46. The distribution of *n*-sided polygons is shown for a temperature of 4.8 K and a field of 320 Oe coarsened with increasing field and temperature, respectively. In both cases, the average number of sides to a cell is six. This propensity for hexagons is consistent with

Euler's theorem[38] stating that the average number of sides in a two-dimensional continuous tiling with *n*-sided cells that have 3-fold vertices is $\bar{n} = 6$. The distribution of *n*-sided cells can be described by a simple triangular distribution function $p_n = 0.5(1 - 0.5|n - 6|)$. This is for the distribution $p_n = C / C_n$, where C is the total number of cells to an area, A, and C_n is the number of *n*-sided cells in that area. Note that p_n is not significantly dependent on temperature or field.

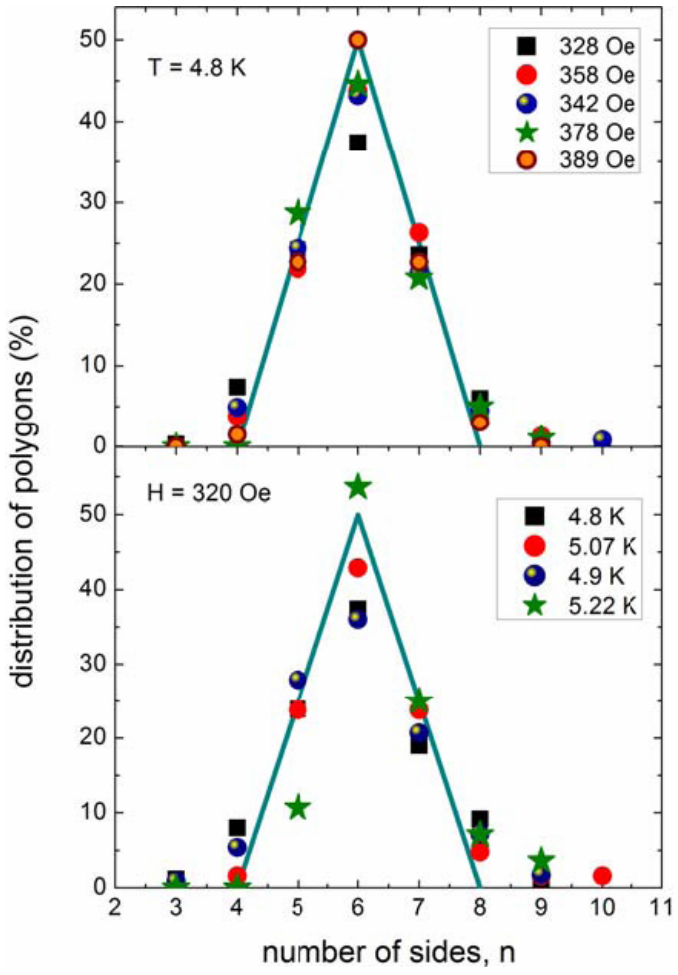

Figure 46. Distribution of *n*-Sided Cells. The top graph was coarsened by increasing field, while the bottom with increasing temperature.

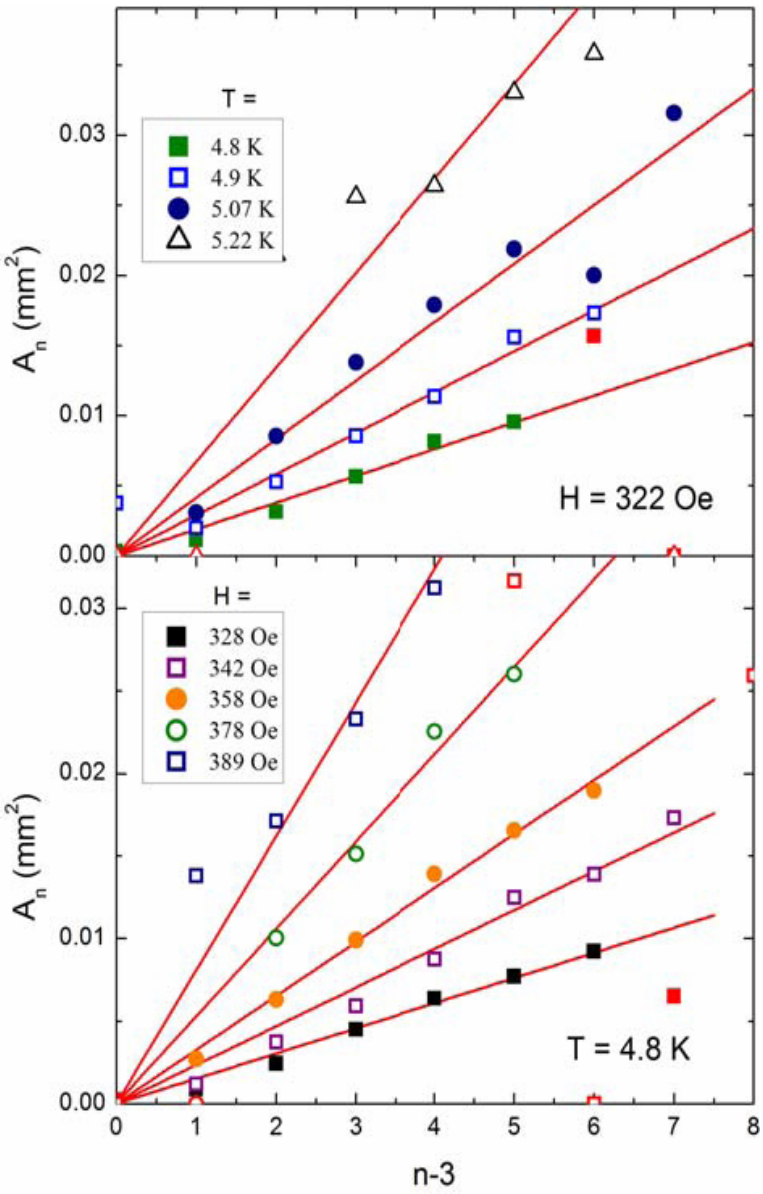

Figure 47. Lewis' Law. These plots show the average area of an n-sided cell vs. the number of sides, n, for a variety of temperatures (top) and fields (bottom).

A common analysis in cellular structures is the average area of an *n*-sided cell, A_n, and its relationship to *n*, the number of sides. This relationship was first studied in biological systems by Lewis who came up with a standard equation known as Lewis' Law[37] $A_n = (A \cdot \lambda / C)(n - [6 - (1/\lambda)])$. Here, λ is a constant that ranges from 1/3 to 1, but is not well understood microscopically. However, von Neumann's Law[39] (discussed later) is believed to

come from the time-dependence of λ. Figure 47 shows the analysis of the suprafroth in terms of the relationship between A_n and n. From these plots an extraction of Lewis' Law, where λ is set equal to 1/3, is possible, giving $A_n = (A/3C)(n-3)$.

The magnetic moment of a volume, V, is $4\pi M = (V/N)(H - H_c) = -V_s \cdot H_c$. Note that the total volume of the superconducting phase inside the intermediate state, V_s, is dependent on the magnetic field and temperature. From the magnetic moment of the volume, one can obtain an equation for the total superconducting wall perimeter $P = (V_s/\delta t) = (A/\delta N H_c)(H_c - H)$ where A is the total area, t is the sample thickness, and δ is the wall thickness which was found by direct measurement to be approximately 10 μm.

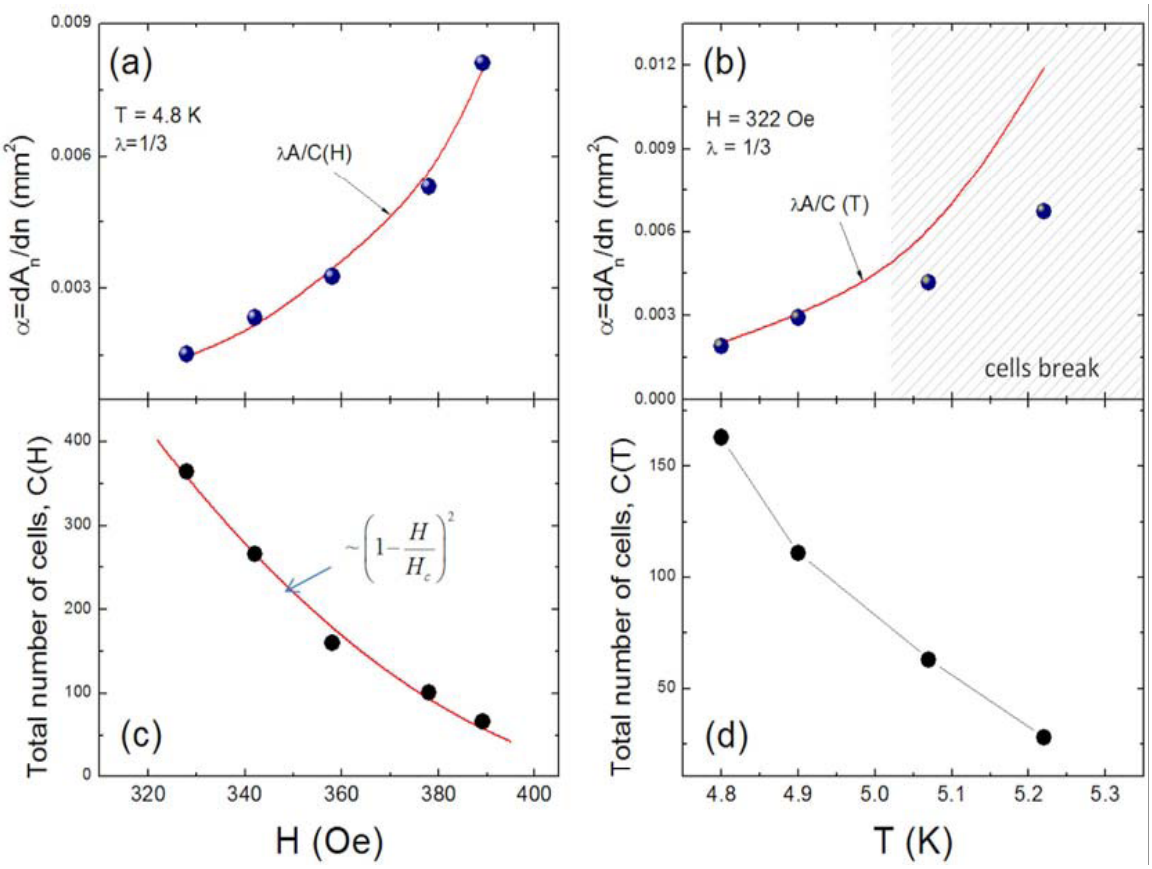

Figure 48. Coefficient of Lewis' Law (top row). Field and Temperature dependence of total C.

The perimeter, P, can be found starting from the distribution, p_n, where $P = C\sum np_n s_n / 2 = 1.85\sqrt{AC}$. For this equation, s_n is the average length of the side of the polygon. From this relation, it is found that $C \sim (H_c - H)^2$. Figure 48(c) shows that this relationship is observed experimentally, and a similar behavior is seen in the temperature dependence (Figure 48(d)). Possibly the most interesting feature here is that the $\lambda = 1/3$ parameter from Lewis' Law plots directly (Figure 48(a)) with the parameter-free calculation of $dA_n / dn = \lambda A / C$, with the experimental values of A and C as shown by the solid line. In Figure 48(b), the deviations from the line are due to cell breaking at the higher temperatures.

Beyond Lewis' Law, however, the von Neumann Law is one of the most commonly studied in reference to the coarsening of froth in foam physics. This law predicts a linear dependence of the rate of change of the area of an n-sided cell to the number of sides of the cell. This relationship has been shown both theoretically and experimentally to be $dA_n / dt = \gamma(n-6)$. The offset of six is historically related to Euler's tiling theorem stating that a hexagon is the most probable polygon. This equation can be generalized for suprafroth. However, we must consider the derivative with respect to field and temperature instead of time. Through a direct differentiation of Lewis' Law with respect to applied field, H, and setting $C = \dfrac{A(H_c - H)^2}{(1.85\delta N H_c)^2}$, it is expected that $\dfrac{dA_n}{dH} = \dfrac{2.28(N\delta)^2}{(1 - H/H_c)^3}(n-3) = \beta(n-3)$.

We can force β to stay fairly constant by not allowing H to vary much (~5%), which in turn makes $H / H_c \approx const$. With an (*n–3*) dependence, our generalized von Neumann law states that even though we have a higher probability of hexagons, any polygon with $n > 3$ will grow in area with an increase in field (and temperature as shown in Figure 49 (bottom)). Figure 49 shows that this is indeed the case where derivatives were evaluated for a small range of fields (and temperatures). By substituting the values of $H=0.8H_c$, $H=0.044\ T$, $\delta=0.014\ mm$, and $N=0.63$, we can arrive at an estimate of $\beta \approx 0.5$, which is very close to the experimental value of *0.6*.

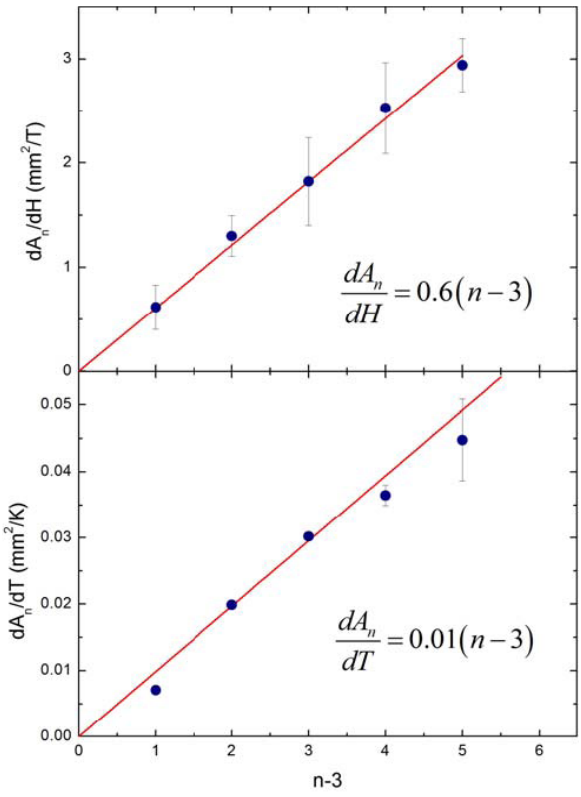

Figure 49. Suprafroth Generalized von Neumann Law. The top image was calculated at 4.8 K, the bottom at 330 Oe.

The dependence of (*n–3*) instead of the normal (*n–6*) dependence can be determined through empirical examination, also. This (*n–3*) dependence is directly related to the methods by which coarsening occurs. In a conventional froth, the amount of froth material remains constant or decreases due to drainage of fluid in processes controlled by surface tension and diffusion of boundaries. In suprafroth, however, the coarsening process is controlled by magnetic pressure inside the cells. Because we are increasing the applied field, the pressure increases on all cells. Therefore, all cells should grow in area with an increase in magnetic field. This is the case as we never see a polygon of *n=3*, and no smaller *n*-value is available.

4. Discussion of the Applied Current Results

In the Experiments chapter, we discussed the motion of the intermediate state flux structure when an external current was applied. As was expected from the Lorentz force, the general flux motion is perpendicular to both the current flow and the direction of the applied magnetic field. However, the reaction of the structure itself has been unexpected. So, from the experiments we performed, a few observations should be made.

While the perpendicular motion of flux was not surprising, when the density of the flux became high enough, the sample entered what was referred to as the "stripe pattern." The flux structure exists purely as rows of flowing flux separated by thin, superconducting lines as shown in Figure 50. This effect was also observed by Solomon and Harris[33] (Figure 51) who then proposed the superconducting domain velocity followed the equation $|v_d| = \frac{J_0 \cdot c}{H_c \cdot \sigma}$, where J_0 is the current density and σ is the normal state electrical conductivity. Our experiments resulted in a normal state flux tube flow on the order of 1 mm/s with a

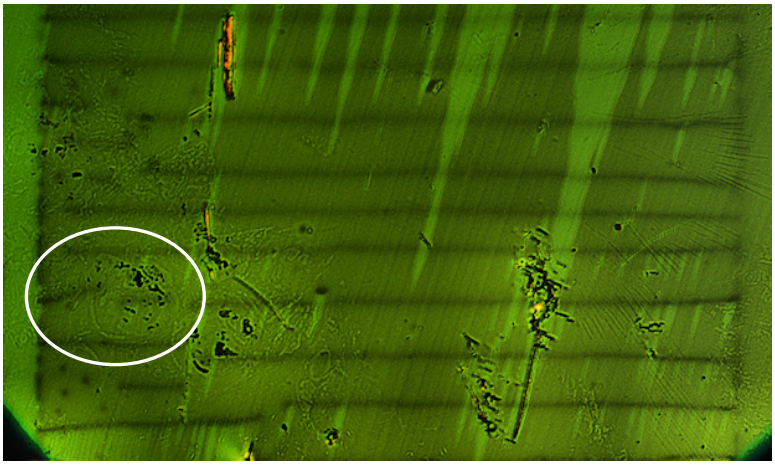

Figure 50. The Stripe Pattern. Circled in white are the broken superconducting domains observed and discussed by Solomon and Harris[33].

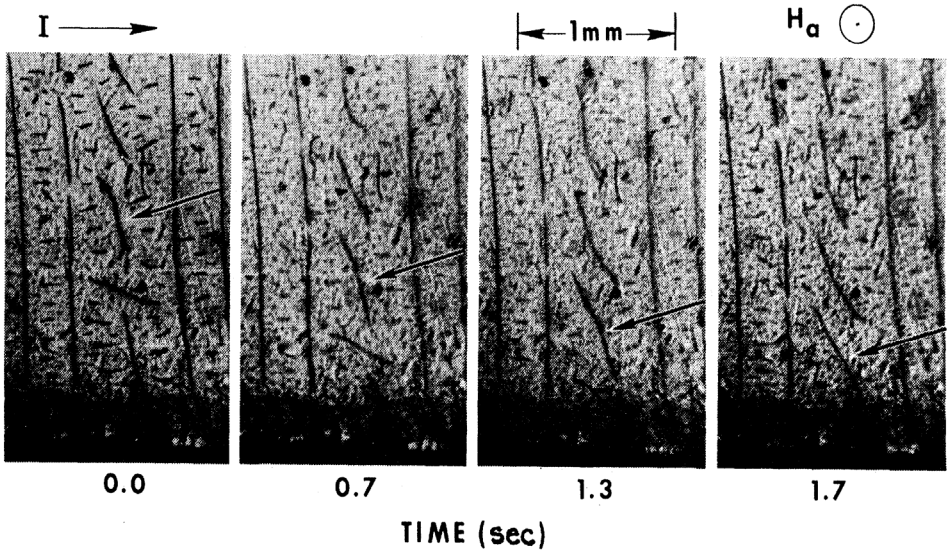

Figure 51. Motion of Superconducting Domains. Observed by Solomon and Harris[33].

maximum measured velocity of 3 mm/s. The question to consider is, "How does the applied current flow through these perpendicular normal laminae?"

When looking at Figure 50, the answer to this question is not obvious. One would believe that, because there is no resistivity, an applied current would only flow through the superconducting regions of the sample. With the majority of superconducting paths perpendicular to the flow of current, though, this may not be the case. It is possible that the current flows directly through the normal domains. This would help explain any heating of the sample with higher applied currents. A second possibility could be that the current only flows along the edges of the samples where there is always a superconducting path (until the sample reaches the normal state). However, this current flow may not provide the Lorentz force needed for the observed perpendicular motion of flux.

Another possible answer to this current flow question lies in the question of whether or not the normal regions we see are actually laminae. Two aspects of our imaging need to be remembered. First, our video is standard video with a frame rate of 30 fps. It is possible that

the motion we see is actually a series of flux tubes that are moving faster than frame rate can catch. In that case, paths may exist for the applied current to flow through. The other experimental aspect to consider is that we are only viewing the surface magnetization of the sample. Concurrently, the flux could move as a series of tubes, allowing current flow throughout the sample, while the flux tubes are merged along the sample surface providing the images that are observed. Without additional experiments with cameras that have faster frame rates, it can not be definitively stated which of these options are occurring.

The experiments have also resulted in the appearance of flux tubes nucleating at the sample edge. Figure 52 shows a sample that was brought to the normal state at a constant current and was then brought back to the intermediate state with a decreasing applied field. Note that when this sample crossed into the intermediate state, the flux structure was that of Figure 50. The applied current has induced a flux tube nucleation at the right edge of the sample and then forced these tubes across the sample, forming the structure that is seen in Figure 52. The likely reason for this nucleation is that the applied current creates its own magnetic field that wraps around the sample, which causes a nucleation akin to the finger

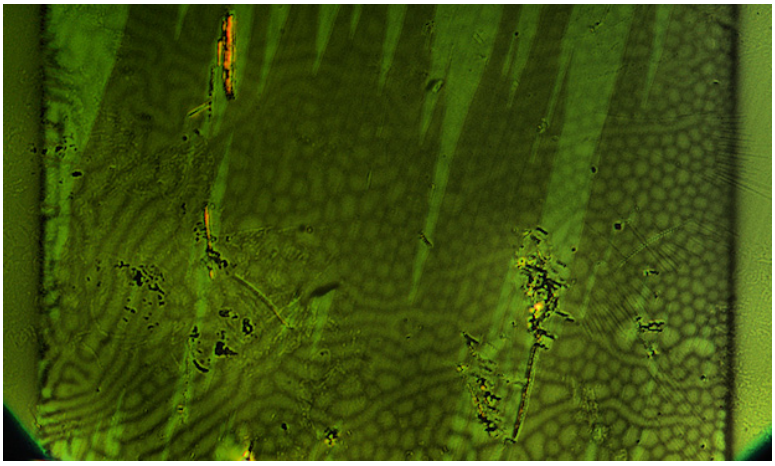

Figure 52. Current Induced Flux Tube Nucleation. The flux tube motion is right to left.

structure tube nucleation discussed earlier (Figure 12).

Through observation of these experiments, I have created an H-I phase diagram. This diagram is shown in Figure 53. All data was taken after ZFC the sample at a constant current and then increasing the applied field. In this diagram, there are six distinct regions. To the left of the black line is the sample's Meissner state. To the right of the black line, the sample is in the intermediate state with an influx of normal tubes, but there is not yet any motion of these tubes. Above the red line, the flux structure has begun to move perpendicular to the applied current. Above the blue line is a small region where there occurs nucleation of tubes at the edge of the sample. Applied currents below 0.35 A were found insufficient in the nucleation of flux tubes. Beyond the green line is the stripe pattern. And, finally, above the

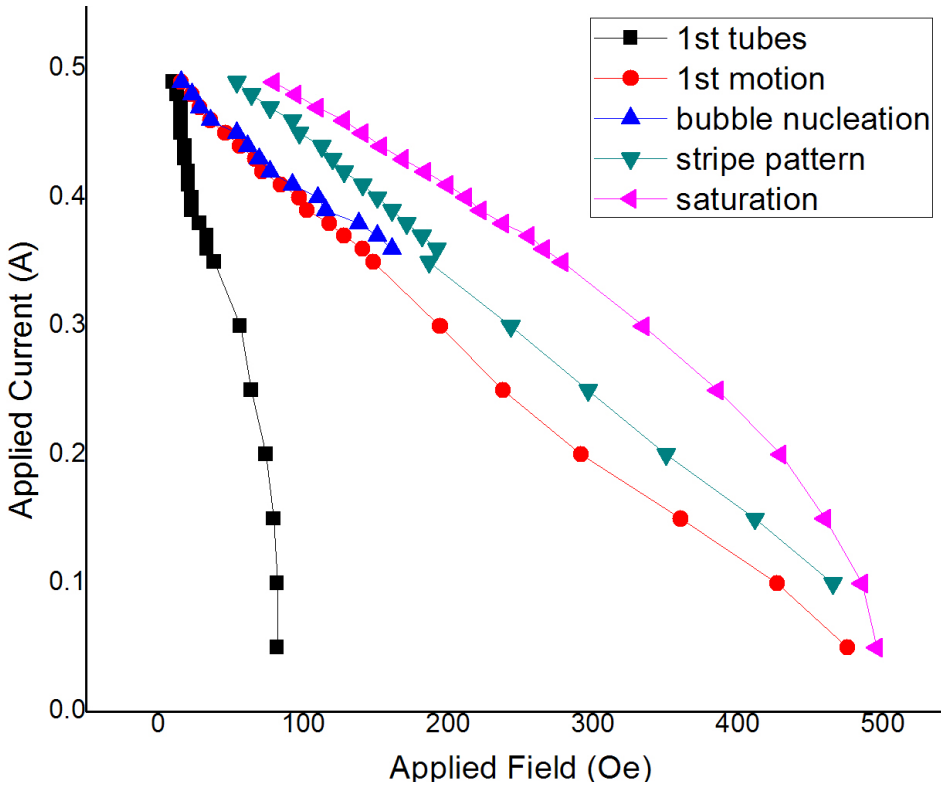

Figure 53. H-I Phase Diagram.

purple line is the normal state of the sample. This H-I phase diagram is representative of every sample we have imaged. An important note, though, is that because I was holding the sample at a constant current for each line of data points, the temperature is constant only over that set of data points. For higher currents, the sample is at a higher (but still constant) temperature. This explains why the black line turns up at higher applied currents.

5. Fast Ramp of the Magnetic Field

Through all of the previous experiments, every effort has been made to keep the change in field both slow and uniform. In this section, the effect of a fast ramp rate[41] on the magnetic structure of the intermediate state is observed.

In Figure 54 I show two different Pb samples. The left image is of a square slab and the right image is of a Pb strip with no current passing through it. Both samples were ZFC and both have had an abrupt increase in the applied magnetic field. As can be seen, even

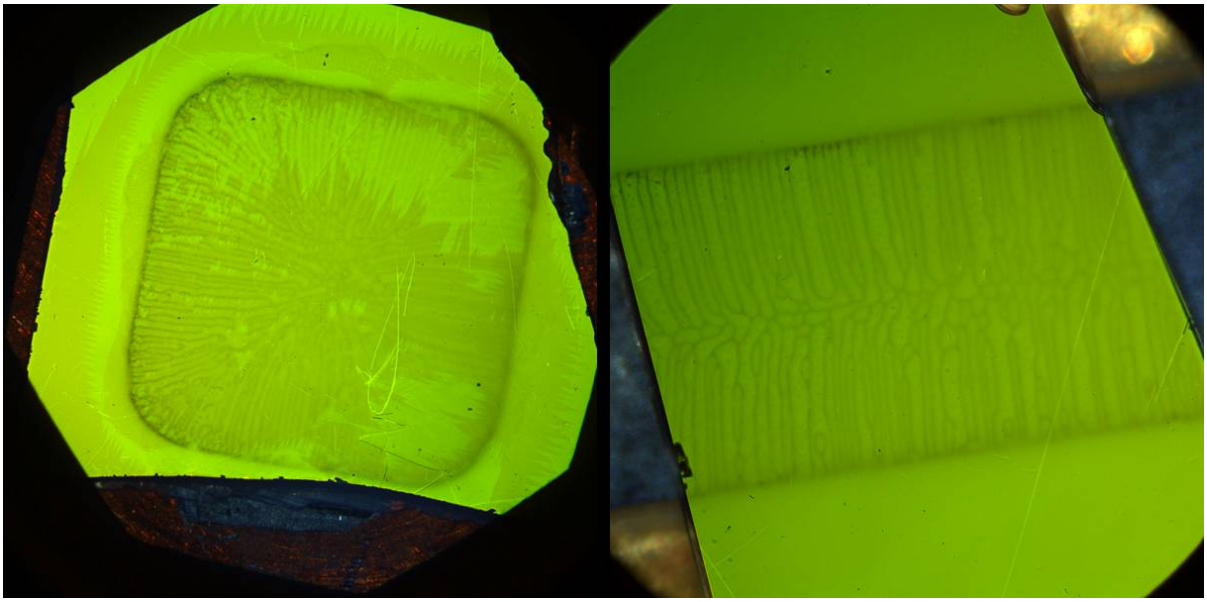

Figure 54. Fast Ramp Effects. Both images show samples that have had the applied field introduced quickly. The left image is a square slab. The right image is a Pb strip.

though both samples have crossed the SI interface, there is little-to-no tubular structure. The flux structure that has appeared seems laminar and is very ordered. All the flux has penetrated perpendicular to the edges of the samples and meets in the sample center where a small amount of tubular structure remains.

To "fast ramp" the magnetic field, I increased the power supply to the desired field, turned the power supply output off, ZFC the sample and then turned the power supply output on again. The result was a fast increase in the magnetic field produced by the solenoid. The effect observed in Figure 54 is dependent on the magnitude of the applied field, not sample geometry. Below a certain field density, the structure resembles that of the slow ramp structure observed previously.

Figure 55 and Figure 56 show the results for both slow and fast ramped applied fields. Figure 55 shows a Pb hemisphere sample and Figure 56 shows the Pb crystal disc. Both series of images show that at lower fields the samples behave independently of the rate of change of the applied field. At higher field densities, however, the samples begin to show very different behaviors between the slow ramp and the fast ramp images. Notice that at near critical fields (Figure 55), both the slow ramp and fast ramp structures consist of superconducting threads. Also, for the higher fields in the Pb disc (Figure 56), remnants of the tubular phase are found in the sample center. This is likely due to the lack of pinning in the Pb disc. The first entrance of flux is able to move fast enough that it still arrives in the center as flux tubes. It should be noted that while not shown, the disc presented the same periodic array of superconducting threads that the hemisphere shows at near critical fields.

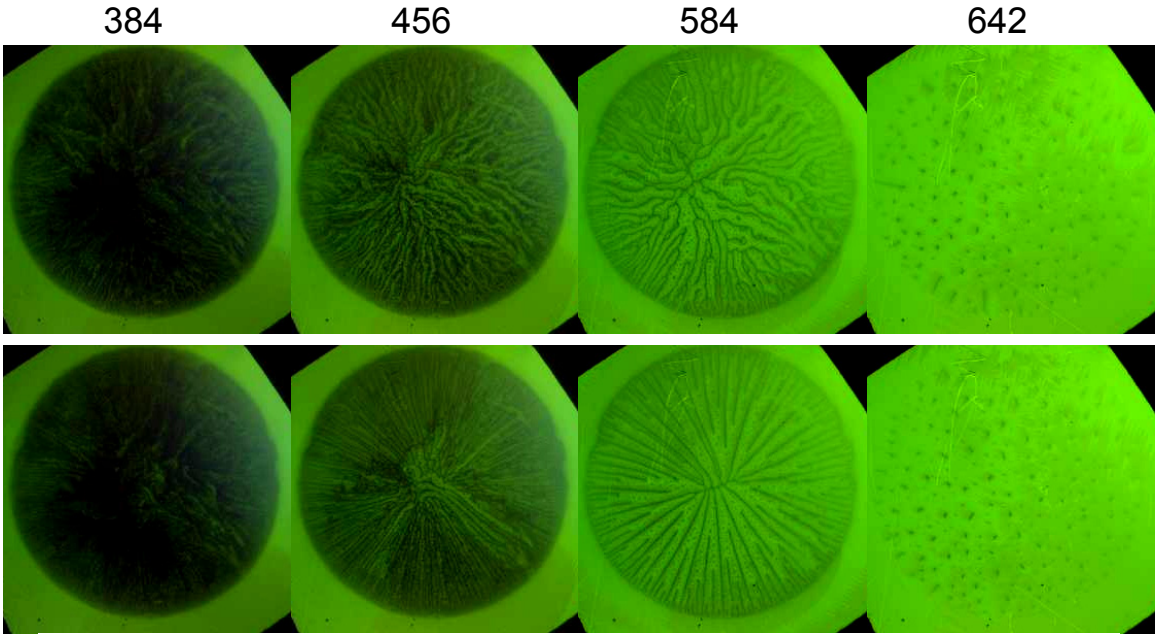

Figure 55. Fast Ramp Hemisphere. The top row shows the flux structure after slowly ramping the applied field. The bottom row shows the structure after fast ramping the same field.

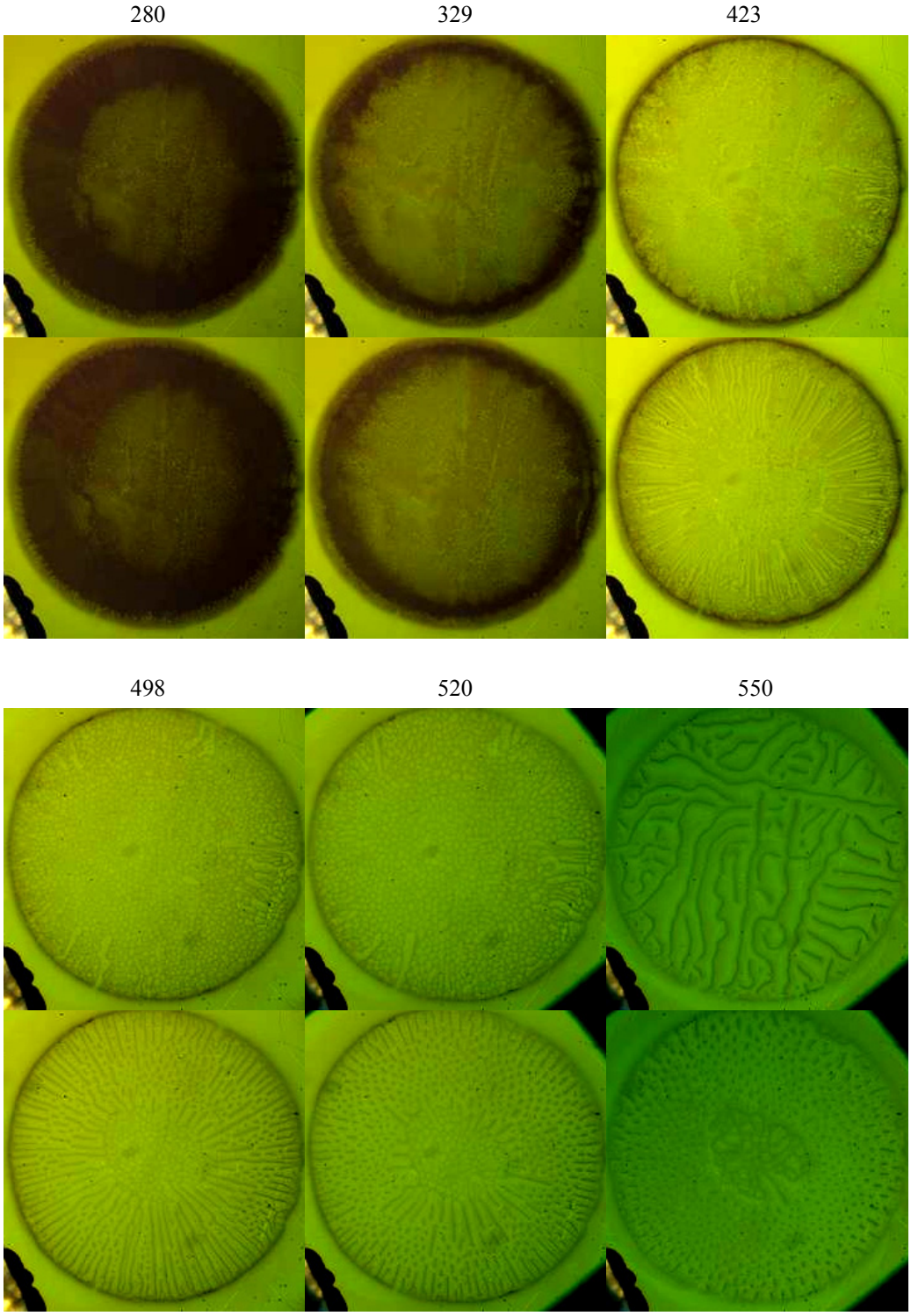

Figure 56. Fast Ramp Disc. In both series of pictures, the top row is the slow ramp image and the bottom row is the fast ramp image.

CHAPTER V. CONCLUSIONS

The original purpose of this research was focused on gaining a greater understanding of the tubular structure in the intermediate state. As was stated before, much of the previous work considered flux tubes a result of pinning and defects. I believe that this work, along with the previous work of our group[20,21,37] proves otherwise. When looking at the MO imaging performed on the samples of different shapes, the tubular structure was prevalent. In our cleanest sample (Figure 9), there exists only the tubular structure until field density no longer permitted it. This structure was found to follow a theoretical model proposed by Goren and Tinkham from over 30 years ago. Additionally, when considering the cone and hemisphere shape samples there existed both laminar and tubular structure at all fields, but the laminar structure is likely due to pinning in these samples. All samples exhibited laminar breakup at low fields during flux exit and the laminar structure has been observed[55] to break into flux tubes as the flux exits a sample with a geometric barrier. Furthermore, when taking a basic energy consideration, there appeared a linear link between the proposed flux tube length and the field applied as the proposed tube traveled into the center of either sample, supporting the existence of only flux tubes in pinning-free samples without a geometric barrier. Samples that have two flat surfaces require no change in the length of flux tubes, resulting in the creation and motion of flux tubes being governed by the current distributions. It is possible that the laminar structure is only brought on by the geometric barrier and the continuity of magnetic flux leaving the sample or by pinning and other defects. This possibility is supported by the measured magnetization loops. When comparing Figure 5 of the Introduction chapter with that of Figure 38 in the Discussion chapter, the magnetic

hysteresis only occurs in the sample that contains the geometric barrier and is presumably the only sample of the two that creates the Landau laminar structure.

We have also seen that at high enough densities, the tubular structure behaves as other well known models in foam physics. This suprafroth structure follows Euler's prediction of the average cell containing six sides. It was also found to follow both Lewis' Law and von Neumann's Law governing cell size and change of cell size with respect to the applied field or temperature. While there are differences inherent in the different methods of coarsening — such as the fact that all suprafroth cells grow, providing an (n–3) dependence instead of the standard (n–6) dependence — there is also a reversibility found in the structure that is not available in conventional froths.

In addition to the application of field alone, an applied current has shown interesting tubular/laminar transitions. As described earlier, there exists a small range of field and current where there is a nucleation of flux tubes, even when there is already a laminar structure established throughout the sample. At higher currents, the structure changes to a stripe pattern perpendicular to current flow.

A structural dependence on the ramp rate at which the magnetic field is applied was also found. At fast ramp rates, the magnetic flux structures were very ordered at high flux densities while lower magnetic densities provided little change to the structure. Also, in all of the samples there was an ordered superconducting thread structure as the applied field, H, approached the critical field, H_c.

Much work still needs to be performed in all of the research areas that I have described. Cleaner samples of shapes without the geometric barrier need to be imaged. While there have been efforts in imaging a Pb crystal hemisphere, a Pb crystal cone should be

imaged as well. These measurements should have a corresponding magnetization measurement when possible. Also, there is still a need for the imaging of a pinning-free Pb strip crystal with an applied current. The effect of slab sample thickness should be studied as well. In light of the prevalence of laminar structure found in strip samples, there might exist a thickness limit where the laminar structure always exists, just as there is a thickness limit where a Type-I superconductor behaves like a Type-II superconductor[13]. Furthermore, the motion of flux due to an applied current should be studied using a high-speed camera. This would provide insight into the flux tube nucleation, the flux tube velocities and the stripe pattern. The evolution of a flux tube in both an increasing and decreasing field should be observed carefully and compared to the predictions of the current loop model. This could lead to a greater understanding of the creation of the flux structure. Finally, further work should be performed in the attempt to understand both the fast ramp and the superconducting thread structures.

BIBLIOGRAPHY

[1]L. D. Landau, Sov. Phys. JETP **7**, 371 (1937).
[2]K. B. W. Buckly, M. A. Metlitski, and A. R. Zhitnitsky, Phys. Rev. Lett. **92** (2004).
[3]A. Sedrakian, Phys.Rev. D **71**, 083003 (2005).
[4]T. C. Halsey, Phys. Rev. C **48** (1993).
[5]J. von Hardenberg, E. Meron, M. Shachak, and Y. Zarmi, Phys. Rev. Lett. **87** (2001).
[6]D. Weaire, F. Bolton, P. Molho, and J. A. Glazier, J. Phys.: Condens. Matter **3**, 2101 (1991).
[7]T. Garel and S. Doniach, Phys. Rev. B **26** (1982).
[8]J. Stavans and J. Glazier, Phys. Rev. Lett. **62** (1989).
[9]Kwok-On Ng and D. Vanderbilt, Phys. Rev. B **52** (1995).
[10]R. Wang, I. M. Syed, G. Carbone, R. G. Petschek, and C. Rosenblatt, Phys. Rev. Lett. **97**, 167802 (2006).
[11]M. Seul, Europhys. Lett. **28**, 557 (1994).
[12]F. Elias, C. Flament, J. C. Bacri, and S. Neveu, J. Phys. I **7**, 711 (1997).
[13]R. P. Huebener, *Magnetic Flux Structures in Superconductors* (Springer-Verlag, Berlin, 2001).
[14]M. Tinkham, *Introduction to Superconductivity* (Dover Books on Physics, New York, 2004).
[15]E. H. Brandt and M. Indenbom, Phys. Rev. B **48** (1993).
[16]D. C. Baird and B. K. Mukherjee, Phys. Rev. B **3** (1971).
[17]R. P. Huebener and D. E. Gallus, Phys. Rev. B **7** (1973).
[18]Ch. Jooss, J. Albrecht, H. Kuhn, S. Leonhardt, and H. Kronmuller, Rep. Prog. Phys. **65**, 651 (2002).
[19]H. Kirchner, Phys. Lett. **30A**, 437 (1969).
[20]R. Prozorov, Phys. Rev. Lett. **98**, 257001 (2007).
[21]R. Prozorov, R. W. Giannetta, A. A. Polyanskii, and G. K. Perkins, Phys. Rev. B **72**, 212508 (2005).
[22]L. A. Dorosinskii, M. V. Indenbom, V. I. Nikitenko, Yu. A. Ossip'yan, A. A. Polyanskii, and V. K. Vlasko-Vlasov, Physica C **203**, 149 (1992).
[23]V. Jeudy, C. Gourdon, and T. Okada, Phys. Rev. Lett. **92**, 147001 (2004).
[24]V. Jeudy and C. Gourdon, Europhys. Lett., **75** (3), 482 (2006).
[25]A. Cebers, C. Gourdon, V. Jeudy, and T. Okada, Phys. Rev. B **72**, 014513 (2005).
[26]C. Gourdon, V. Jeudy, and A. Cebers, Phys. Rev. Lett. **96**, 087002 (2006).
[27]V. Jeudy, C. Gourdon, A. Cebers, and T. Okada, J. Appl. Phys. **101**, 09G118 (2007).
[28]V. Jeudy and C. Gourdon, J. Magn. Magn. Mater. **300**, 101 (2006).
[29]J. Provost, E. Paumier, and A. Fortini, J. Phys. F **4**, (1974).
[30]H. Castro, L. Rinderer, and B. Dutoit, Physica C **282-287**, 2343 (1997).
[31]H. Castro, B. Dutoit, A. Jacquier, M. Baharami, and L. Rinderer, Phys. Rev. B **59**, 596 (1999).
[32]R. E. Goldstein, D. P. Jackson, and A. T. Dorsey, Phys. Rev. Lett. **76,** 3818 (1996).
[33]P. R. Solomon and R. E. Harris, Phys. Rev. B **3** (1971).
[34]P. R. Solomon, Phys. Rev. **179** (1969).
[35]R. N. Goren and M. Tinkham, J. Low Temp. Phys. **5**, 465 (1971).
[36]A. Fortini and E. Paumier, Phys. Rev. B **5**, 1850 (1972).

[37]R. Prozorov, A. F. Fidler, J. R. Hoberg, and P. C. Canfield, Nature Phys. **4**, 327 (2008).
[38]D. Weaire and S. Hutzler, *The Physics of Foams* (Oxford Univ. Press, New York, 1999).
[39]R. D. Macpherson and D. J. Srolovitz, Nature **446**, 1053 (2007).
[40]D. Weaire and S. Hutzler, Physica A **257**, 264 (1998).
[41]V. Jeudy, C. Gourdon, and T. Okada, AIP Conf. Proc. **850**, 985 (2006).
[42] C. R. Reisin and S. G. Lipson, Phys. Rev. B **61**, 4251 (2000).
[43] A. T. Dorsey and R. E. Goldstein, Phys. Rev. B **57**, 3058 (1998).
[44]E. Zeldov, A. I. Larkin, V. B. Geshkenbein, M. Konczykowski, D. Majer, B. Khaykovich, V. M. Vinokur, and H. Shtrikman, Phys. Rev. Lett. **73**, 1428 (1994).
[45]A. Meshkovsky and A. Shalnikov, Zh. Eksperim. I Teor. Fiz. **11**, 1 (1947).
[46]A. Fortini and E. Paumier, Phys. Rev. B **14**, 56 (1976).
[47]M. Benkrauda and J. R. Clem, Phys Rev. B **53**, 5716 (1996).
[48]E. H. Brandt, Physica B **284**, 743 (2000).
[49]A. A. Elistratov, O. A. Bobrikov, I. L. Maksimov, and V. Jeudy, Mod. Phys. Lett. B **18**, 19 (2004).
[50]H. A. Leupold, J. J. Winter, and J. T. Breslin, J. Appl. Phys. **41**, 3679 (1970).
[51]M. Menghini, R. J. Wijngaarden, A. V. Silhanek, S. Raedts, and V. V. Moshchalkov, Phys. Rev. B **71** (2005).
[52]M. Menghini and R. J. Wijngaarden, Phys. Rev. B **72** (2005).
[53]M. Menghini and R. J. Wijngaarden, Phys. Rev. B **75** (2007).
[54]A. Hernandez and D. Dominguez, Phys. Rev. B **72** (2005).
[55]P. R. Solomon and R. E. Harris, *United Aircraft Research Laboratories, videotape provided by Dr. N. D. Goldenfeld* (1971).

ACKNOWLEDGEMENTS

I would like to take this opportunity to express my deep gratitude toward those who have provided help in the various aspects of my research and in writing my thesis. First and foremost, I thank Dr. Ruslan Prozorov for his guidance, his constant encouragement and his support through the last two years. His personal investment in my work and good-natured attitude made the work infinitely more enjoyable. I would also like to thank Dr. Paul C. Canfield for his contributions toward and discussions about suprafroth. Additionally, I would like to thank Andrew F. Fidler, Julie Yaouanc and Erick Blomberg for their assistance in the research and analysis that has lead to this thesis. I would like to thank Hal Sailsbury as well, for his help in the sample creation process. Finally, I would like to thank my family and friends for all their support in my endeavors, with a special thanks to Elizabeth Kruesi for her support in my work as well as her editing contributions.